Dynamic evolution of dayside magnetopause reconnection locations and their dependence on IMF cone angle: 3-D global hybrid simulation

Yongyuan Yi[1, 2, 3], Yu Lin[3, a)], Meng Zhou[1, 2, b)], Ye Pang[2], Xiaohua Deng[2]

[1]School of Physics and Materials Science, Nanchang University, Nanchang 330031, People's Republic of China

[2]Institute of Space Science and Technology, Nanchang University, Nanchang 330031, People's Republic of China

[3]Physics Department, Auburn University, Auburn, AL, USA

[a)]Author to whom correspondence should be addressed: linyu01@auburn.edu

[b)]Author to whom correspondence should be addressed: monmentum82@gmail.com

Abstract

We study the dynamic evolution of dayside magnetopause reconnection locations and their dependence on the interplanetary magnetic field (IMF) cone angle via 3-D global-scale hybrid simulations. Cases with finite IMF B_x and B_z but B_y=0 are investigated. It is shown that the dayside magnetopause reconnection is unsteady under quasi-steady solar wind conditions. The reconnection lines during the dynamic evolution are not always parallel to the equatorial plane even under purely southward IMF

conditions. Magnetopause reconnection locations can be affected by the generation, coalescence, and transport of flux ropes (FRs), reconnection inside the FRs, and the magnetosheath flow. In the presence of an IMF component B_x, the magnetopause reconnection initially occurs in high-latitude regions downstream of the quasi-perpendicular bow shock, followed by the generation of multiple reconnection regions. In the later stages of the simulation, a dominant reconnection region is present in low-latitude regions, which can also affect reconnection in other regions. The global distribution of reconnection lines under a finite IMF B_x is found to not be limited to the region with maximum magnetic shear angle.

Plain Language Summary: The channel of solar wind energy transfer into the magnetosphere is widely believed to be controlled by magnetic reconnection at the dayside magnetopause. Understanding the location of dayside magnetopause reconnection is crucial to comprehending the energy coupling process between the solar wind and the magnetosphere. Magnetopause reconnection has been intensively investigated by numerical simulations and space observations. Nevertheless, the locations and dynamic evolution of reconnection sites in the 3-D magnetopause reconnection under different IMF conditions are barely scrutinized. In this paper, we investigate the effects of IMF B_x on the motion of

magnetopause reconnection locations by using 3-D global hybrid simulations under a southward IMF B_z. We find that the reconnection is highly variable due to local magnetopause processes associated with the generation, coalescence, and transport of FRs, as well as reconnection inside the FRs. Under southward IMF conditions with IMF B_x, the magnetopause reconnection initially occurs downstream of the quasi-perpendicular bow shock but eventually dominates in low-latitude regions, including the magnetopause downstream of the quasi-parallel bow shock.

Key points

1. Dayside magnetopause reconnection is highly variable but the reconnection locations eventually maintain quasi-steady in the low latitude.
2. In the presence of IMF Bx, high-latitude dayside reconnection can be inhibited by reconnection near the equator and magnetosheath flow.
3. Variations of reconnection locations are also controlled by the generation, coalescence, and transport of FRs, and reconnection inside FRs.

1. Introduction

Magnetic reconnection is a fundamental space plasma process that

results in abrupt magnetic topology change and acceleration and heating of charged particles. It is widely considered to be a major mechanism for solar wind mass, momentum, and energy to enter the magnetosphere (Dungey, 1961; Lyon, 2000), most efficient under southward interplanetary magnetic field (IMF) conditions (Akasofu, 1981; Lu et al., 2013). Numerous reconnection events have been observed to place at the dayside magnetopause (e.g., Paschmann, 1997; Trattner et al., 2007, 2012a, 2012b, 2016; Anekallu et al., 2013; Burch & Phan, 2016; Pritchard et al., 2019; Fu et al., 2019; Dong et al., 2020; Zou et al., 2022; Man et al., 2022; Qiu et al., 2022). Reconnection sites represent the potential locations where energy conversion and transfer occur. Thus, understanding the location of dayside magnetopause reconnection is crucial to the comprehension of the coupling between the solar wind and the magnetosphere.

Previous studies indicate that the factors affecting the reconnection locations mainly include the orientation of the IMF, the dipole tilt angle, and local dynamic processes. The prevailing view is that the region where the geomagnetic field and the IMF are antiparallel is the most likely location for magnetic reconnection (Dungey, 1961;1963; Luhmann et al., 1984; Trattner et al., 2005). Under southward IMF conditions without a B_x component, the reconnection line tends to be somewhat more equator-aligned near the subsolar region during strong reconnection

(Palmroth et al., 2006; Laitinen et al., 2007; Tan et al., 2012). Trattner et al. (2007) found that the dayside reconnection lines generally tend to be located in an antiparallel reconnection scenario, i.e., where the magnetic shear angle is maximum, under the condition of a southward IMF B_z and a strong IMF B_x. But for the cases with a strong IMF B_y, reconnection at the magnetopause is not limited to regions where magnetic fields are strictly antiparallel, i.e., it can take place in the form of component reconnection.

Previous MHD simulations and observations indicate that positive (negative) B_x results in a northward (southward) shift of the magnetopause reconnection line location (Peng et al., 2010; Tang et al., 2013; Hoilijoki et al., 2014; Pi et al., 2018), that is, reconnection prefers to occur downstream of the quasi-perpendicular bow shock (corresponding to the anti-parallel magnetic field geometry). In the presence of the IMF B_y component, the reconnection line rotates with the IMF clock angle (Palmroth et al., 2006; Laitinen et al., 2007). The tilt of the subsolar reconnection line relative to the equatorial plane is determined by the ratio B_y/B_z of the IMF (Trattner et al., 2007).

Global simulations (Russell et al., 2003; Park et al., 2006; Tan et al., 2011; Cnossen et al., 2012; Hoilijoki et al., 2014; Komar et al., 2015; Guo et al., 2020) and observations (Trattner et al., 2007; Zhu et al., 2015; Kitamura et al., 2016) show that under southward IMF conditions, the

reconnection locations along the dayside magnetopause tend to shift toward the winter hemisphere from the subsolar region due to the effect of the geomagnetic dipole tilt. Positive (negative) dipole tilt angle contributes to the southward (northward) moving of the reconnection line location, consistent with the season effect proposed by Trattner et al. (2007).

Utilizing 2-D global hybrid simulations, Omidi et al. (2006, 2007) and Hoilijoki et al. (2017, 2019) studied the magnetopause reconnection and flux transfer events (FTEs) under southward IMF conditions, and found that time-dependent reconnection leads to the formation of multiple X-lines and FTEs at the low-latitude magnetopause during steady IMF conditions. Omidi et al. (2006, 2007) showed that the initiation of reconnection is due to local current sheet thinning and intensification which may be affected by the shock-related ULF waves and ion tearing within the current sheet. Hoilijoki et al. (2017, 2019) further emphasized that despite steady solar wind conditions, the location and rate of reconnection at the X-lines exhibit significant variability due to magnetosheath turbulence, neighboring X-lines, and the motion of magnetic islands.

Similar dynamic features were obtained in 3-D global hybrid simulations. Tan et al. (2011, 2012) showed that both multiple X-line reconnection and single X-line reconnection coexist at the magnetopause.

Under the purely southward IMF configuration, the segments of X-lines on the dayside magnetopause are approximately parallel to the equatorial plane. Guo et al. (2020) found that neighboring reconnection sites could impact the local plasma conditions at the magnetopause. The generation and propagation of FRs, the magnetosheath flows, and the outflow structures associated with multiple reconnection sites significantly modulate the positions of X-lines. Although recursive FRs form and propagate poleward, the average locations of the magnetopause subsolar X-lines remain nearly the same.

To date, 3-D global hybrid simulations have been used to explore many important features of the dynamic evolution of magnetopause reconnection, e.g., the evolution of FRs (Guo et al., 2020; Guo et al. 2021a, 2021b, 2021c) and the generation of kinetic Alfvén waves (Wang et al., 2019). The hybrid simulations include ion kinetic physics self-consistently in the global dynamics. However, no hybrid simulations have specifically examined the impact of the IMF conditions on the evolution of reconnection locations at the 3-D magnetopause. MHD simulations do not include the charged particle dynamics and the turbulent magnetosheath structures due to ion kinetic physics. On the other hand, while in situ spacecraft observations of the structure of reconnection (Russell & Elphic, 1978; Phan et al., 2004; Yan et al., 2016; Wang et al., 2017a; Pritchard et al., 2019; Zou et al., 2022; Zhong et al.,

2023) as well as the turbulent structures of its ambient magnetosheath (Huang et al., 2017; Yao et al., 2018; Wang et al., 2018; Wang et al., 2019; Li et al., 2020; Shi et al., 2021) have shown that dayside magnetopause reconnection and its location may be unsteady under turbulent magnetosheath conditions, observations are limited in their ability to infer the existence of extended reconnection lines because the spacecraft generally sample a limited region during one passage of the reconnection region. It is difficult for observations to provide a complete time-dependent structure of the entire region where reconnection may be occurring.

In this paper, we investigate the dayside magnetopause reconnection locations, their dynamic evolution, and their dependence on IMF B_x by using 3-D global hybrid simulations under a southward IMF B_z. The purpose is to achieve a better understanding of the location and motion of the dayside reconnection X-line. The outline of the paper is as follows. In Section 2, we briefly introduce the simulation model. Section 3 introduces our method to identify the magnetopause surface and the reconnection locations. The simulation results are presented in Section 4. Elaborate discussions and the summary are given in section 5 and section 6, respectively.

2. Simulation model

We perform 3-D dayside global hybrid simulations (Lin et al., 2005, 2006, 2007; Pang et al., 2010) to investigate the effect of IMF B_x on magnetopause reconnection. The detailed numerical scheme is described by Swift (1996). In the hybrid code, ions are treated as particles, electrons are treated as a massless and isothermal fluid. Ion motion is given by Newton's equation under Lorentz force. The electric field is obtained from the electron momentum equation. Electron flow velocity is evaluated from Ampere's law. Magnetic field is advanced in time following Faraday's law. A spherical coordinate system (r, θ, φ) is employed in the simulation. The simulation results are described in the geocentric solar-magnetospheric (GSM) coordinate system, in which the X-axis points from the Earth to the Sun, the Z-axis is in the plane containing X and geomagnetic dipole axis and pointing northward, and the Y-axis completes the right-handed system. More details of this code can be found in Lin & Wang (2005).

In all cases to be shown, the ion gyrofrequency Ω_0 in the solar wind is chosen to be 1.0 s^{-1}, corresponding to an IMF of ~10 nT, where $\Omega_0 = eB_0/m_i$. The solar wind ion inertial length, $d_{i0} = c/\omega_{pi0,}$ is chosen to be 0.1 R_E. Note that the Alfvén speed in the solar wind is $V_{A0}= d_{i0}\,\Omega_0$. The solar wind flow speed is $V_0 = 5V_{A0} = 0.5$, corresponding to a solar wind Alfven Mach number $M_A=5$. The ion plasma beta is $\beta_i=0.5$ and electron plasma beta $\beta_e=1$ in the solar wind, and the ion number density in the solar wind

is N_0=12000. The simulation grids are uniformly distributed in the north-south and east-west directions, which contain 104 and 130 grid points, respectively. Nonuniform grid spacing Δr is employed in the radial direction, with a higher spatial resolution from r = 8 R_E to 13 R_E, encompassing the magnetopause boundary layer, magnetosheath, and bow shock regions. In these areas, the grid size is approximately equal to $1d_{i0}$, while it is ~$1.3d_{i0}$ for r > 13 R_E. Outflow open boundary conditions are applied at the backside planar boundaries (X = 0), while a perfect conducting boundary is implemented at the inner boundary at r = 4 R_E.

All the results are presented in normalized units. The magnetic field B is normalized to the IMF B_0, the flow velocities are normalized to the solar wind Alfvén speed V_{A0}, the electric field is expressed in units of $V_{A0}B_0$, the ion number densities are normalized to the solar wind density N_0, the time t is normalized to Ω_0^{-1}, and the spatial coordinates are expressed in units of R_E.

The IMF cone angle is defined as the angle between the +X axis and the IMF, i.e., $\alpha = \arccos(|\mathbf{B_0} \cdot \mathbf{X}|/\mathbf{B_0})$. Here $\mathbf{B_0}$ = (B_{x0}, B_{y0}, B_{z0}) is the IMF. In this paper, 3 cases with different IMF cone angles are presented. Case 1 is based on a purely southward IMF with $\mathbf{B_0}$= (0, 0, -1), and thus $\alpha = 90°$. The other two cases have a non-zero IMF B_{x0} component. In case 2, $\mathbf{B_0}$= (-0.707, 0, -0.707), and thus $\alpha = 45°$; case 3 also has $\alpha = 45°$, but B_{x0}<0, i.e., $\mathbf{B_0}$= (0.707, 0, -0.707).

3. Methods

3.1 Identification of the dayside magnetopause surface

Figures 1a and 1b show an example of how we identify the magnetopause locations. Plotted in the figure are the contours of magnetic field component B_z in the Y=0 and Z=0 planes obtained from case 1 with a purely southward IMF. The positive B_z corresponds to the northward magnetospheric field, the negative B_z in high latitudes on the tailward side of the positive B_z ($X < 6$) corresponds to the southward magnetospheric field, and the negative B_z on the sunward side of the positive B_z represents the southward magnetosheath and IMF B_z. We identify the dayside magnetopause surface, indicated by the black dashed lines in Figures 1a and 1b, by the location of the reversal of magnetic field component B_z as it turns southward from the northward magnetospheric field, similar to the MHD simulation study of Němeček et al. (2011). Figures 1c and 1d show the line cuts of magnetic field component B_z and Y-component current density, $J_{y,}$ as a function of X along the Sun-Earth line (Y=0 and Z=0). The location of B_z reversal is found to coincide with the location of the current density peak, as shown by the red dashed lines in Figures 1c and 1d. In this study, we do not utilize the streamline method as in Palmroth et al. (2003, 2006) and Lu et al. (2011). This is because our focus is solely on the dayside

243 magnetopause, defined as the magnetopause regions on the sunward side
244 of the cusp, under southward IMF B_z conditions. The B_z component can
245 be used to directly mark the sunward side of the cusp region (positive
246 magnetospheric B_z). Here, the search for the magnetopause surface is
247 carried out in the planes at constant Y, from Y=-10 to Y=+10 with an
248 interval of $\Delta Y=0.2$. In each of these planes, the search starts from Z=-10
249 to Z=+10 with an increment of $\Delta Z=0.2$ to locate the X position of the B_z
250 reversal at each Z value. The 3-D magnetopause position is then obtained
251 at various times. As seen in the line cut profiles shown in Figures 1c and
252 1d, the current density (J_y) peaks around the magnetopause location of B_z
253 reversal.

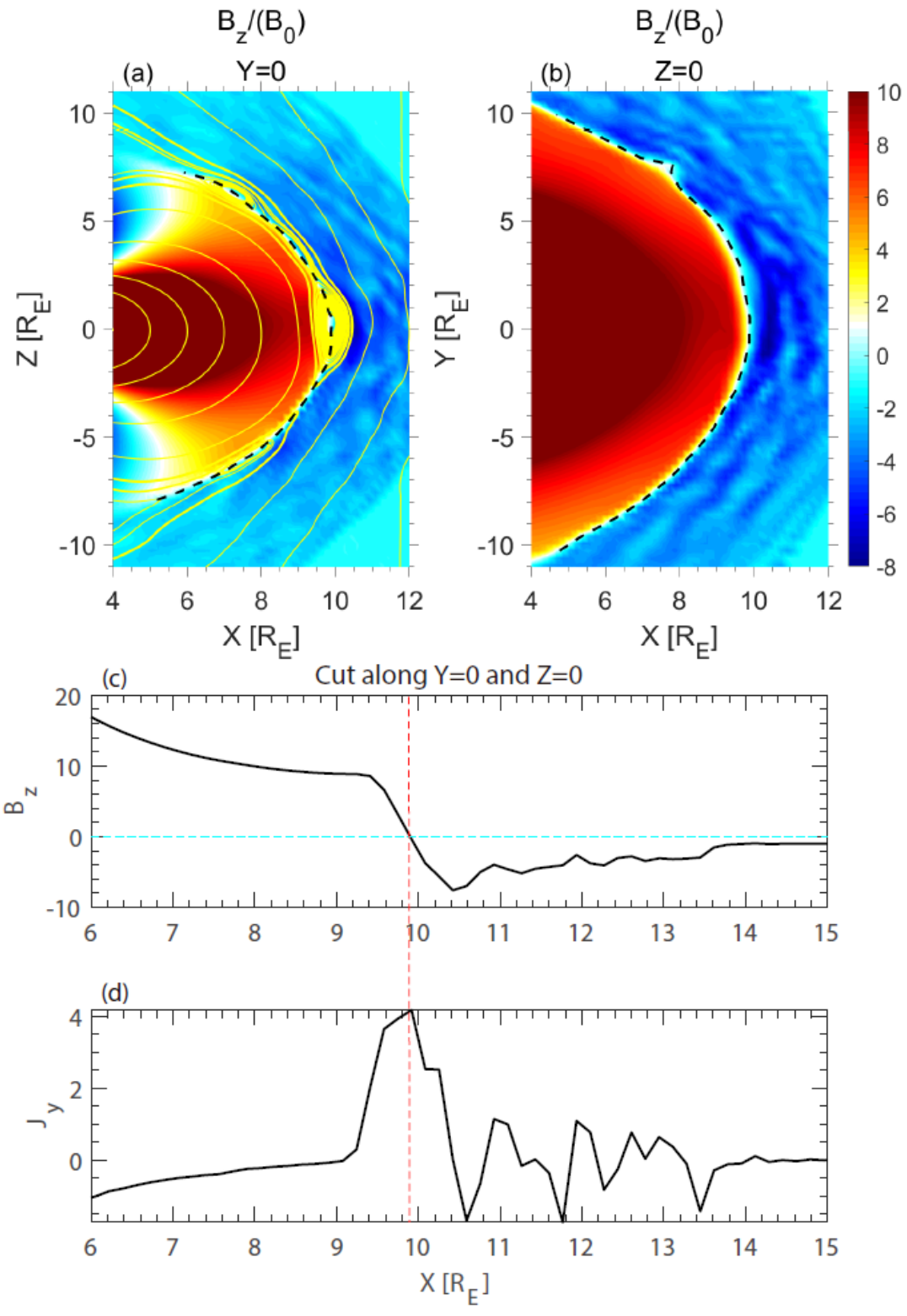

Figure 1. Contours of magnetic field component B_z in the noon-meridian plane (a) and equatorial plane (b) at t=60. Line cuts of B_z component (c) and current density J_y (d) as a function of X along Y=0 and Z=0. The

black dashed curves in Figures 1a and 1b and the red vertical dashed lines in Figures 1c and 1d mark the magnetopause location.

3.2 Identification of the reconnection location

After the dayside magnetopause surface is identified, we can search for the reconnection location along the magnetopause following the method of Tan et al. (2011) and Guo et al. (2020). There are several commonly used criteria for the identification of local X-lines. We take the noon-meridian plane to show an example of our approach in Figure 2, which plots the contours of ion bulk flow velocity ($\mathbf{V_p}$) component V_{pz}, magnetic field component B_y, non-ideal energy conversion term $\mathbf{J}\cdot(\mathbf{E}+\mathbf{V_p}\times\mathbf{B})$, and the 2-D projection of magnetic field lines in the noon-meridian plane. First, based on the magnetic field directions surrounding the X-point (the red mark 'X' inside each of the three red boxes in Figure 2a), we can classify four types of field lines near an X-point: closed field lines of northward magnetic field on the earthward side of the magnetopause current sheet ($B_z>0$), open field lines of southward magnetosheath field on the sunward side of the current sheet ($B_z<0$), reconnected field lines connecting the magnetosheath field and dipole field with a sunward $B_x>0$, and the reconnected field lines with an earthward $B_x<0$. Second, near the X-point, bidirectional ion bulk flow velocities V_{pz} pointing away from the X-point are present, corresponding

to the reconnection outflows. Third, the presence of an asymmetric quadrupole Hall magnetic field (B_y) in the vicinity of the X-point (Figure 2b) with stronger B_y perturbations on the magnetosheath side of the magnetopause boundary layers, while similar features are also observed by MMS spacecraft (Peng et al., 2017; Wang et al., 2017b; Zhang et al., 2017). The asymmetric Hall structure of B_y appears clearly around the X-line in the red boxes around Z ~ ±3 and Z ~ +5. Fourth, strong non-ideal energy conversion takes place as seen from the positive $\mathbf{J}\cdot(\mathbf{E}+\mathbf{V_p}\times\mathbf{B})$ in the red boxes in Figure 2c, which has frequently been used to identify the diffusion region of reconnection (e.g., Zenitani et al., 2011; Burch et al., 2016; Zhong et al., 2021; Zhou et al., 2017, 2019, 2021).

The local reconnection X-points can be identified by the above features. However, the asymmetric Hall magnetic field structures are not always obvious due to the contamination of the B_y perturbations in flux ropes and the turbulent magnetosheath (Mozer et al., 2008; Pritchett, 2008; Shay et al., 2016; Tanaka et al., 2008; Dai et al., 2016). Besides, it is difficult to provide explicit criteria for identifying the global X-lines based on the non-ideal energy conversion, for the non-ideal energy conversion not only occurs in X-point. In this work, we focus on the global distribution of the dominant dayside magnetopause reconnection regions with V_{pz} reversal (e.g., the X-lines at Z~ ±3 in Figure 2a,). Relatively weak

reconnection without V_{pz} reversal (as shown in Figure 2a, the X-line at Z~ +5) which quickly propagates away from the dayside region (Hoilijoki et al., 2017; Guo et al., 2020) due to strong background convection (including magnetosheath flows) (Tanaka et al., 2010) is not the focus of this article. The ion outflow V_{pz} reversals and the B_x component reversals along the +Z direction in the magnetopause surface (B_z~0) are mainly used to identify the reconnection locations. The Hall field and non-ideal energy conversion are only used to assist in the identification. The search for the reconnection locations is carried out in the planes at constant Y, from Y=-10 to Y=+10 with an increment of ΔY=0.2. The global distribution of reconnection locations on the dayside magnetopause is then obtained.

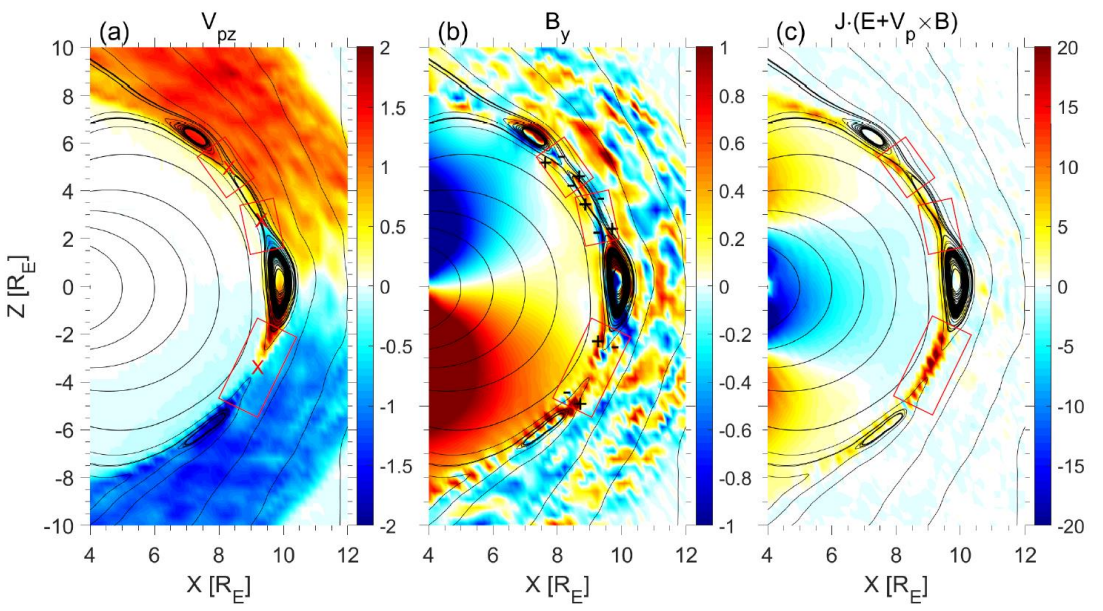

Figure 2. Contours of (a) Ion bulk flow velocity component V_{pz}; (b) magnetic field component B_y; and (c) non-ideal energy conversion term $\mathbf{J}\cdot(\mathbf{E}+\mathbf{V_p}\times\mathbf{B})$ in the noon-median plane. The red mark "X" in (a)

represents the X-point we identified. The red boxes represent the ion diffusion region.

4. Simulation Results

4.1 Temporal evolution of reconnection locations under purely southward IMF

Figure 3 shows the evolution of magnetopause magnetic field lines configuration and reconnection locations (small black circles) under a purely southward IMF in case 1 from t=5 to t=145. At t=5, dayside magnetopause reconnection occurs first at the subsolar region around the equatorial plane, which is due to the solar wind dynamic pressure and IMF geometry. Only one reconnection line (continuous reconnection locations) is present (Figure 3a). However, as the simulation progresses, the magnetopause reconnection locations become more dynamic due to the presence of multiple X-lines (Tan et al., 2011, 2012; Guo et al., 2020; Guo et al., 2021a, 2021c). The number of reconnection lines increases to more than two after t=5, with three reconnection points being present in some planes of constant Y, as seen in Figures 3b-3e.

At t=20, multiple small-scale flux ropes (FRs) are formed in the vicinity of the equator, which subsequently transport to high-latitude regions or evolve into larger-sized FRs. As shown in Figure 3c, a large

FR with a scale of more than 5 R_E in the Z direction is generated between two continuous reconnection lines due to multiple X-line reconnection located around the subsolar region, spanning from Y=-5 to Y=5. Three main reconnection lines nearly parallel to the equator are shown at this stage (t=60), with one located from Y=-10 to Y=-5 near the equator, the second from Y=-5 to Y=+5 near Z=+2 north of the equator, and the third from Y=-5 to Y=+10 near Z=-5 south of the equator. Some FRs, however, become tilted toward the Z direction because the propagation speeds of FRs (associated with the plasma flow velocity at the magnetopause) are different. The reason for the varied propagation speed is due to the occurrence of different dynamic processes at different Y distances, which will be discussed in Section 5, Discussions. As a result, the long reconnection lines split into multiple segments, as shown in Figure 3d at t=100.

An obvious consequence is that the X-lines are no longer parallel to the equatorial plane, especially on the dawn side. As for the dusk side, the reconnection lines do not change much due to the presence of the steady reconnection line from Y=-5 to Y=10 near Z=-5 south of the equator. But later at t=145, most of the reconnection locations are seen to have shifted back to the vicinity of the equatorial plane (Figure 3e). The reason for the shift is due to the occurrence of strong reconnection near the equator, and reconnection in the high-latitude region

propagates to the cusp and dissipates, which will be also discussed in Section 5 as well. The average locations of reconnection at the low-latitude regions maintain a quasi-steady state and vary north and south between Z=-5 and Z=+5 with the time-dependent FRs, as also shown by Guo et al. (2020). This finding indicates that the reconnection locations undergo temporal variations and are influenced by local dynamic processes, even under steady upstream solar wind conditions. Furthermore, the 3-D reconnection process exhibits greater complexity in the out-of-plane (i.e., dawn-dusk) direction.

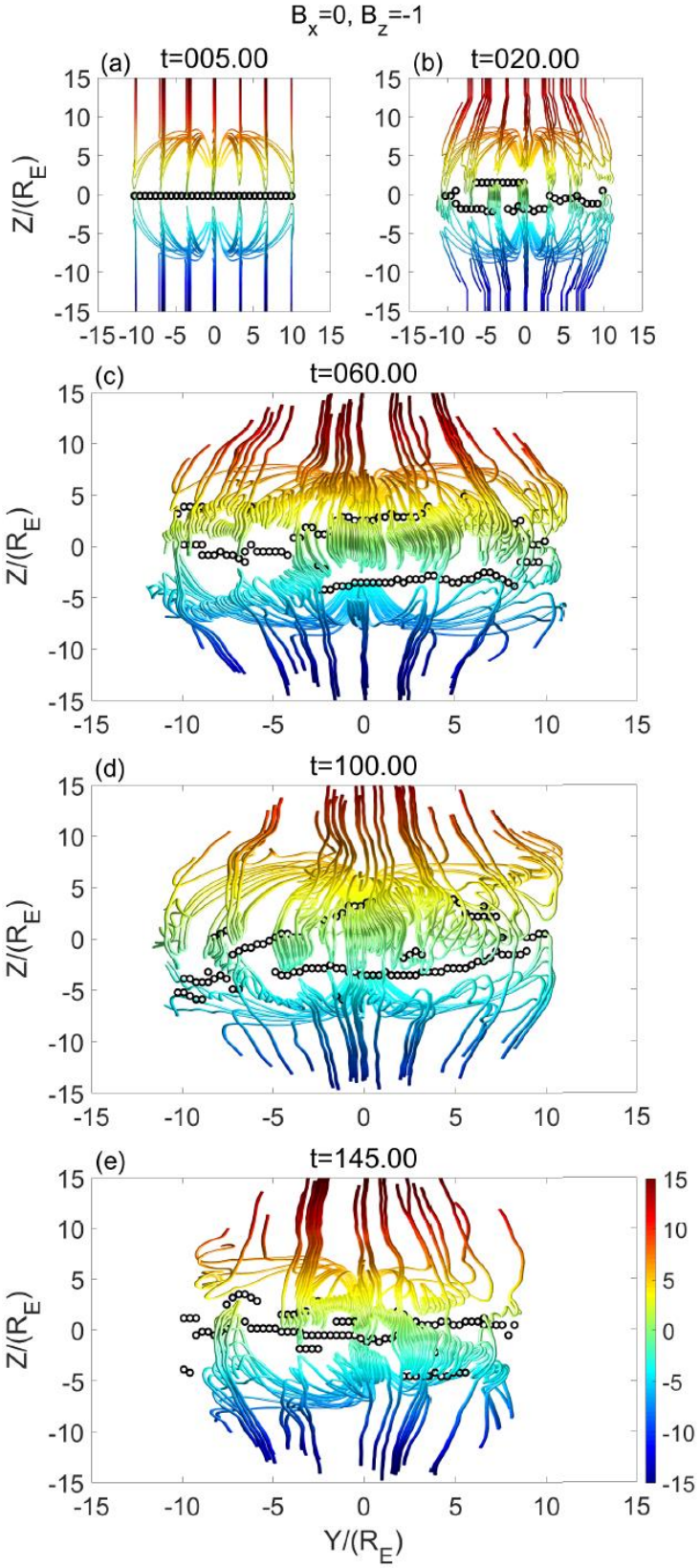

371

372 Figure 3. Temporal evolution of the spatial 3D magnetopause magnetic

373 field line configuration and the reconnection locations in case 1 at (a) t=5,

(b) t=20, (c) t=60, (d) t=100, and (e) t=145. The small black circles represent the locations of reconnection X-points in the planes at various constant Y. The magnetic field lines are color-coded according to the Z coordinate.

4.2 Effects of IMF cone angle on reconnection locations

Figure 4 shows the time evolution of magnetopause field line configuration and the reconnection locations in case 2 from t=5 to t=100, in which a finite and negative IMF B_x (with cone angle of 45^o) is imposed. At t=5, reconnection is observed only in the southern high-latitude regions around Z=-5 (Figure 4a), downstream of the quasi-perpendicular bow shock, where the geomagnetic field and magnetosheath field are antiparallel. With the dynamic evolution of magnetopause reconnection, the reconnection locations become variable due to the generation and propagation of FRs. It is shown that the FRs are initially formed in the high-latitude regions, as a result of the increase in the number of reconnection points around the early reconnection line. As seen in Figure 4b, two or three X-points are present in the X-Z planes at t=40, and the reconnection locations have shifted towards both higher and lower latitudes. Subsequently at t=60 (Figure 4c), subsolar reconnection has started, and reconnection structures in the high-latitude regions gradually disappear. Only reconnections around the subsolar region are still active.

Similar processes have also occurred in the ±Y direction following that in the subsolar region, and most of the reconnection locations at different Y eventually shift to the low-latitude regions (Figure 4d). At t=100, magnetopause reconnection also appears downstream of the quasi-parallel shock, as seen from the FRs around Y=-5 to Y=5 in Figure 4d.

Figure 5 shows the evolution of the magnetopause magnetic field line configuration and the reconnection locations in case 3. In this case, which is similar to case 2 but with an opposite IMF with $B_x>0$, reconnection first takes place only in the northern high-latitude regions, corresponding to, again, downstream of the quasi-perpendicular bow shock (Figure 5a). The evolution of X-lines is similar to that in case 2, that is, the reconnection locations gradually shift to the low-latitude regions (Figures 5b-5d). In general, the average locations of reconnection maintain a quasi-steady state in the low-latitude regions in the later stage of the simulation, regardless of the sign of IMF B_x.

It is noteworthy that, although foreshock waves are generally found upstream of the quasi-parallel shock (northern high-latitude regions in case 2 and southern high-latitude regions in case 3) (e.g., Hoppe et al., 1983; Russell & Hoppe, 1983; Scholer et al., 1990; Lin & Wang, 2005; Lin et al., 2007; Wang et al., 2009; Shi et al., 2017; Liu et al., 2019), which lead to turbulent electromagnetic field in the magnetosheath

(waggled field lines in Figures 4b-4d and 5b-5d) than that downstream of the quasi-perpendicular bow shock (southern high-latitude regions in case 2 and northern high-latitude regions in case 3), we do not find significant reconnection in the magnetopause (satisfies our criteria described in section 3) triggered by the magnetosheath turbulence. Such results indicate that a more turbulent magnetosheath condition does not necessarily result in a higher occurrence rate of magnetopause reconnection, consistent with the observations by Petrinec et al. (2022).

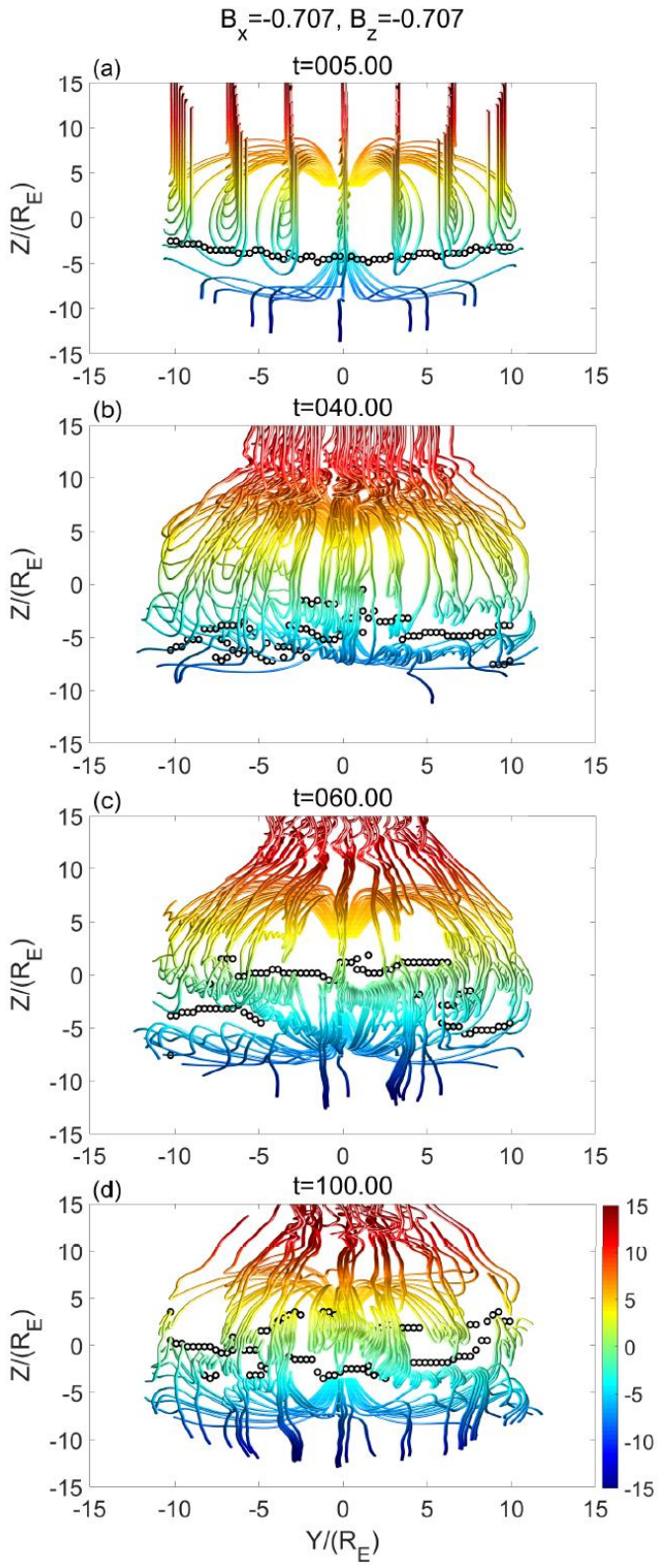

Figure 4. Temporal evolution of the spatial 3D magnetopause magnetic field line configuration and the reconnection locations in case 2 with B_x=-0.707 and B_z=-0.707 at (a) t=5; (b) t=40; (c) t=60, and (d) t=100, in

the same format as Figure 3.

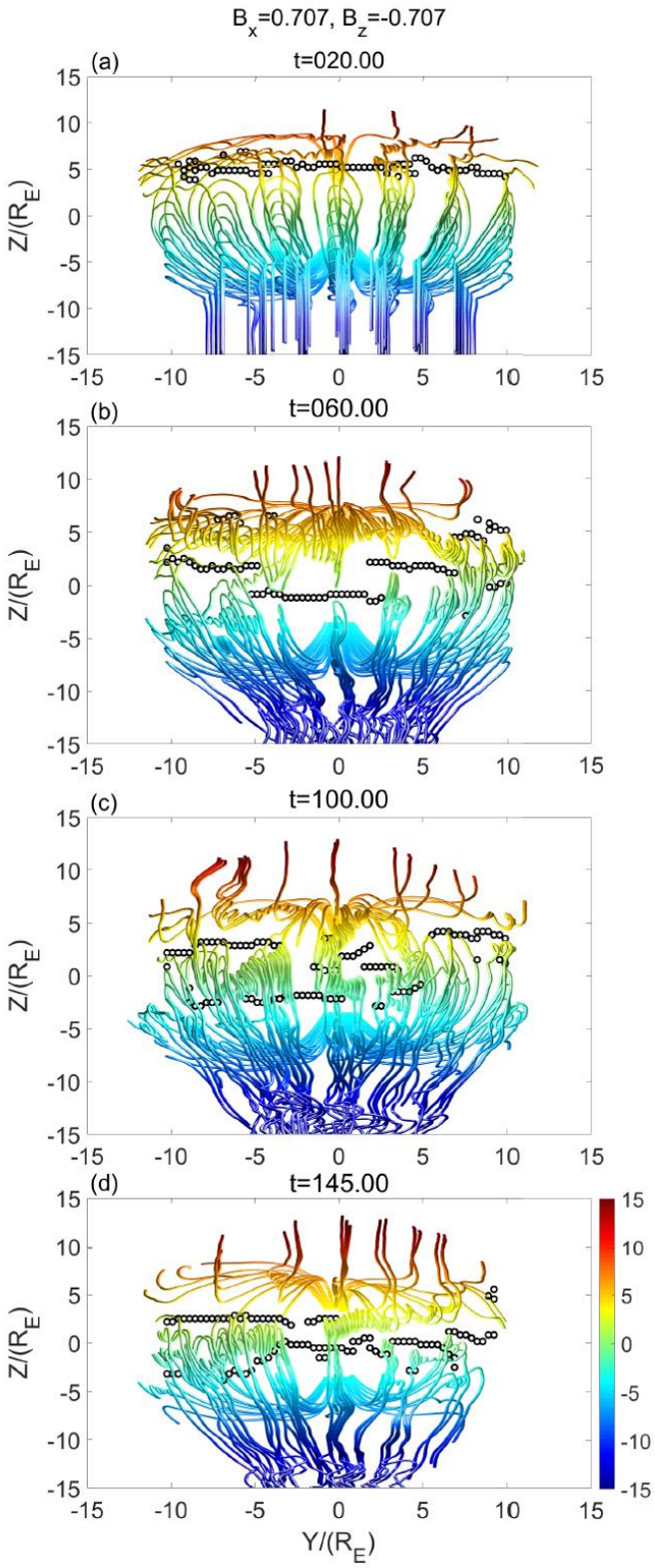

Figure 5. Temporal evolution of the magnetopause magnetic field line configuration and the reconnection locations in case 3 with B_x=0.707 and

434 B_z=-0.707 at (a) t=20; (b) t=60; (c) t=100, and (d) t=145, in the same
435 format as Figure 3.
436
437 **4.3 Magnetic field shear angle and the reconnection locations**
438 In order to understand the global locations of magnetopause
439 reconnection, we compare the simulated reconnection locations with the
440 antiparallel reconnection scenario. Figures 6a and 6b show the magnetic
441 field shear angles between the magnetosheath and magnetospheric
442 magnetic field lines, θ_{shear}, at t=60 projected onto the magnetopause
443 surface for case 1 and case 2. Here, $\theta_{shear}=\cos^{-1}(\mathbf{B_p}\cdot\mathbf{B_s}/(|\mathbf{B_p}||\mathbf{B_s}|))$, $\mathbf{B_p}$
444 represents the magnetospheric magnetic field, $\mathbf{B_s}$ the magnetosheath
445 magnetic field, and the angle θ_{shear} >145° represents a near antiparallel
446 configuration. Note that in our cases with a finite IMF B_x but a zero B_y, a
447 smaller magnetic shear angle does not necessarily mean component
448 reconnection, but rather a larger normal component of magnetic field B_x.
449 As expected, the majority of the dayside magnetopause surface is
450 characterized by the maximum magnetic shear conditions (θ_{shear}>145°) in
451 both cases with a southward IMF. Reconnection locations (black circles)
452 are mainly distributed across the regions characterized by the maximum
453 (i.e., near antiparallel) magnetic shear conditions (θ_{shear}~145° to 180°) on
454 the dayside magnetopause, consistent with previous studies by Dungey
455 (1961) and Trattner et al. (2005, 2007). However, we also find that the

reconnection locations on the dawn and dusk sides, where the magnetic shear angles are between 90° and 145°. We find reconnection here is consistent with the component reconnection scenario, in which the magnetospheric and magnetosheath magnetic fields have a large common guide field component.

Figures 6c-6d show the magnetopause ion bulk flow velocity component V_{pz} as viewed from the Sun. We also find that compared with the antiparallel magnetic field configuration, the reversal of the ion bulk flow velocity component V_{pz} can provide a better indication of the reconnection locations in these cases under a southward IMF and without IMF B_y, including both the dawn side and dusk side regions. By examining the changes in V_{pz} and its reversal across the magnetopause surface, we can pinpoint the regions where significant reconnection is taking place under the southward IMF conditions.

In order to understand the large magnetic shear angle among the southern and northern regions of the dayside magnetopause shown in Figure 6b in the presence of IMF B_x, we examine the time evolution of the field line configuration. Figures 6e and 6f present the ion bulk flow component V_{pz} in the noon-meridian plane together with the projected magnetic field lines at t=20 and t=60, respectively, in case 2 with a negative IMF B_x. At t=20, magnetopause flow reversal occurs in the southern hemisphere (Z=-5 in Figure 6e), where the field lines between

478 the magnetospheric and magnetosheath are antiparallel. On the other hand,
479 in the northern hemisphere, the field lines between the magnetosphere
480 and magnetosheath do not exhibit a large magnetic shear angle, and the
481 shear angle decreases with the increase of latitude due to the initial IMF
482 B_x conditions (θ_{shear}~145° at the equator). It is found that the
483 corresponding current sheet is thicker in the northern hemisphere than in
484 the southern hemisphere, as can be seen by the loose magnetic field lines
485 in the northern hemisphere (Figure 6e). Since the magnetosheath field
486 lines undergo compression by the solar wind (Kivelson & Russell, 1995;
487 Lopez et al., 2017; Madelaire et al., 2022), the shocked IMF lines are
488 highly curved along the dayside magnetopause, and a thinner
489 magnetopause current sheet is present downstream of the
490 quasi-perpendicular shock where the magnetic shear angle is large. At
491 t=60, antiparallel reconnection (θ_{shear}>145°) also occurs in both the
492 southern and northern hemispheres (Figures 6b and 6f), equatorward of
493 the original reconnection location at Z=-5. The global reconnection
494 locations thus appear to have shifted equatorward. As shown in Figure 6f,
495 the reversal of ion bulk flow velocity component V_{pz} shifts to Z=+1 at
496 t=60. Although the field configuration is still antiparallel in the southern
497 hemisphere, the X-line in the southern hemisphere is suppressed by the
498 southward outflow from the newly formed reconnection region at Z=+1.
499 In the later stage, the reconnection locations are no longer controlled by

the initial IMF conditions, but rather by the local magnetopause dynamic processes. Overall, reconnection prefers to occur over a broad range of the magnetopause.

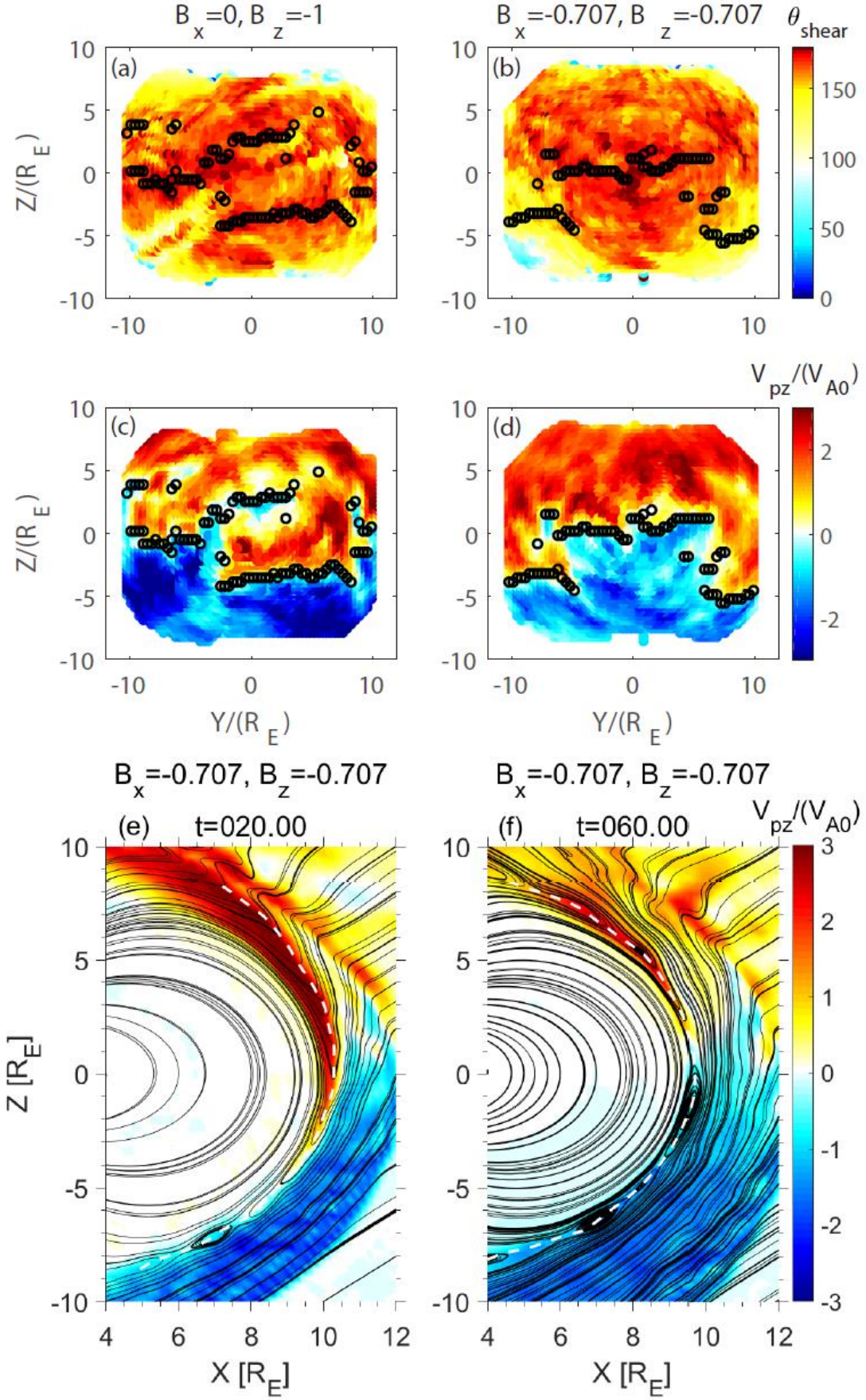

503

504 Figure 6. Earth's magnetopause color-coded for the magnetic shear angle

between the magnetosheath and magnetospheric field lines (a-b) and the ion bulk flow velocity component V_{pz} (c-d) under different IMF B_x at t=60 as viewed from the Sun; the ion bulk flow velocity component V_{pz} and the 2-D view of magnetic field lines in the noon-meridian plane at t=20 (e) and t=60 (f). (a) and (c): B_x=0, B_z=-1; (b), (d), (e), and (f): B_x=-0.707, B_z=-0.707. The black circles in (a)-(d) represent the reconnection locations. The white dashed lines at (e)-(f) represent the magnetopause surface.

5. Discussions

Our hybrid simulations have shown that the dayside magnetopause reconnection is unsteady. During the dynamic evolution even under steady solar wind conditions, the reconnection locations are not simply determined by the maximum magnetic shear location on the basis of the initial IMF direction. How does the location of reconnection evolve dynamically? In the following, we discuss some reasons for the shift of reconnection locations.

5.1 Effects of Flux Ropes

Early diagrams of dayside reconnection typically depict a single quasi-steady reconnection site, as first proposed by Dungey in 1961. However, observations indicate that dayside reconnection often occurs in

bursts, forming FRs that are commonly observed at the magnetopause, as reported by Russell and Elphic (1978), Kawano and Russell (1997), Fear et al. (2007, 2012), and Wang et al. (2006). In general, reconnection can occur at a single X-line or multiple X-lines. Figures 3b-3c, 4b-4d, and 5b-5d also show the same processes that single X-line reconnection becomes multiple X-line reconnection during the temporal evolution, and the reconnection locations shift northward or southward from the original site.

In addition, the coalescence of the FRs can also change the magnetic field topology and the variation/shift of reconnection locations. Figures 7a-7c show the time evolution of contours of ion bulk flow component V_{pz} and the 2-D view of magnetic field lines during the coalescence of FRs in the Y=-3.2 plane in case 1. At t=60, a reconnection X-line is seen to be located at Z=+2, and a southward-moving FR (FR1) is on the southern side of this X-line, as indicated in Figure 7a. Then, at t=65, a new reconnection X-line is generated at Z=-5, and a new magnetic flux rope (FR2) is formed on the northern side of FR1, subsequently merging with FR1 (Figure 7b). At t=70, the X-line at Z=+2 has disappeared with only one FR left. The above results are supported by the 3-D field lines presented in Figure 8.

Figures 7d-7e show the line cuts of the magnetic field component B_x and ion flow component V_{pz} along the magnetopause surface at t=65 in

549 the Y=-3.2 plane. Both B_x and V_{pz} between FR1 and FR2 reverse from
550 positive to negative along the +Z direction, though their reversal locations
551 are not exactly the same. It is shown that V_{pz} inside FR1 and at the
552 merging point near Z=-0.8 is positive, which means that FR1 is moving
553 northward to merge with FR2. As a result, the reconnection outflow of the
554 X-line at Z=+2 is gradually suppressed by the northward-moving flow. At
555 t=70, only the X-line at Z=-5 survives. It is found that the reconnection
556 location can change by 7 R_E in the Z direction, spanning between the
557 northern and southern hemispheres.

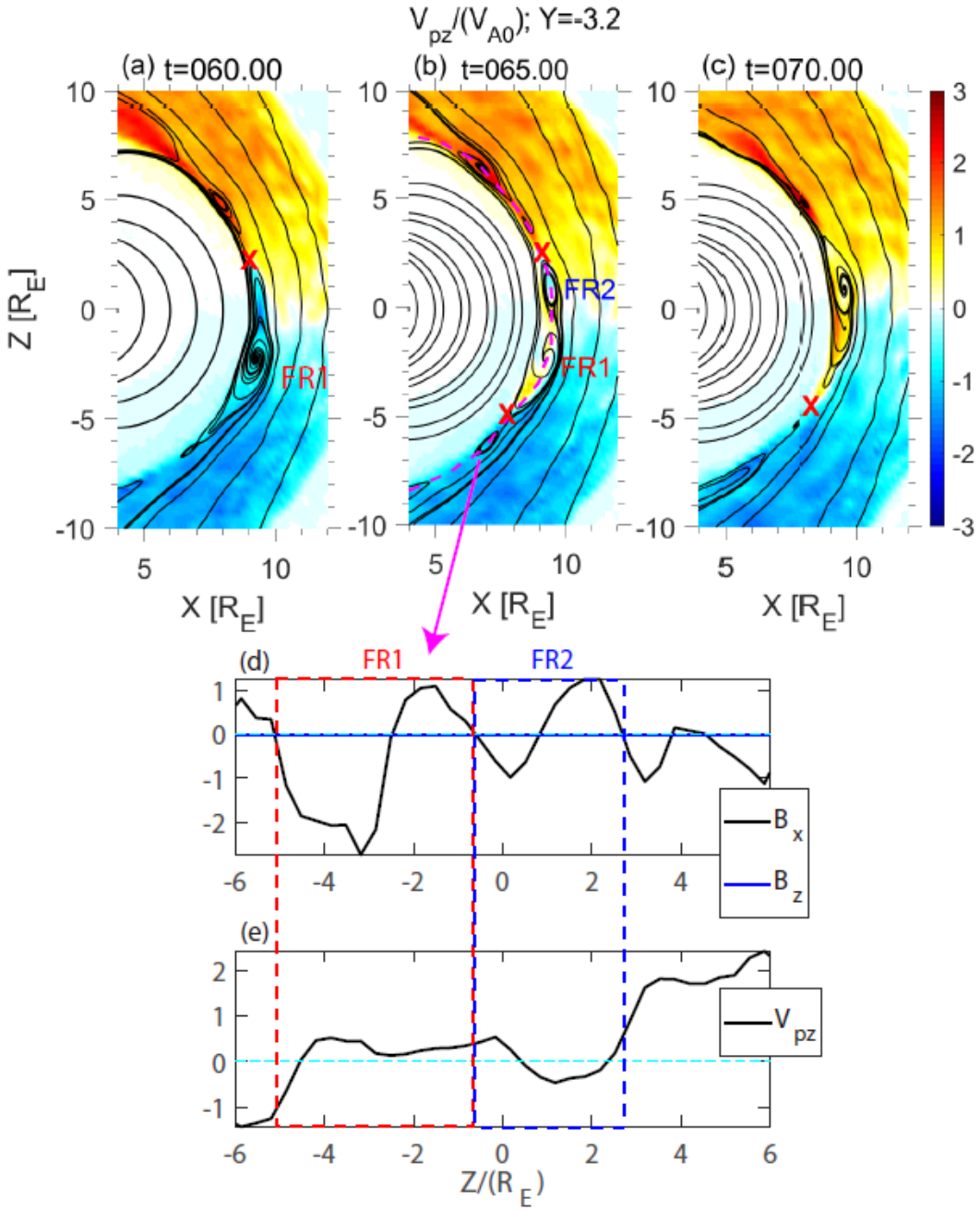

Figure 7. Coalescence of FRs in case 1. Contours of ion particle bulk velocity component V_{pz} at t=60 (a), t=65 (b), and t=70 (c); the line cuts of magnetic field components B_x, B_z (d), and ion bulk velocity component V_{pz} (e) along the magnetopause surface at t=65 in the Y=-3.2 plane. The red mark 'X' represents the location of V_{pz} reversal from negative to positive along the +Z direction. The red and blue dashed boxes in Figures

7d and 7e represent the flux ropes FR1 and FR2, respectively.

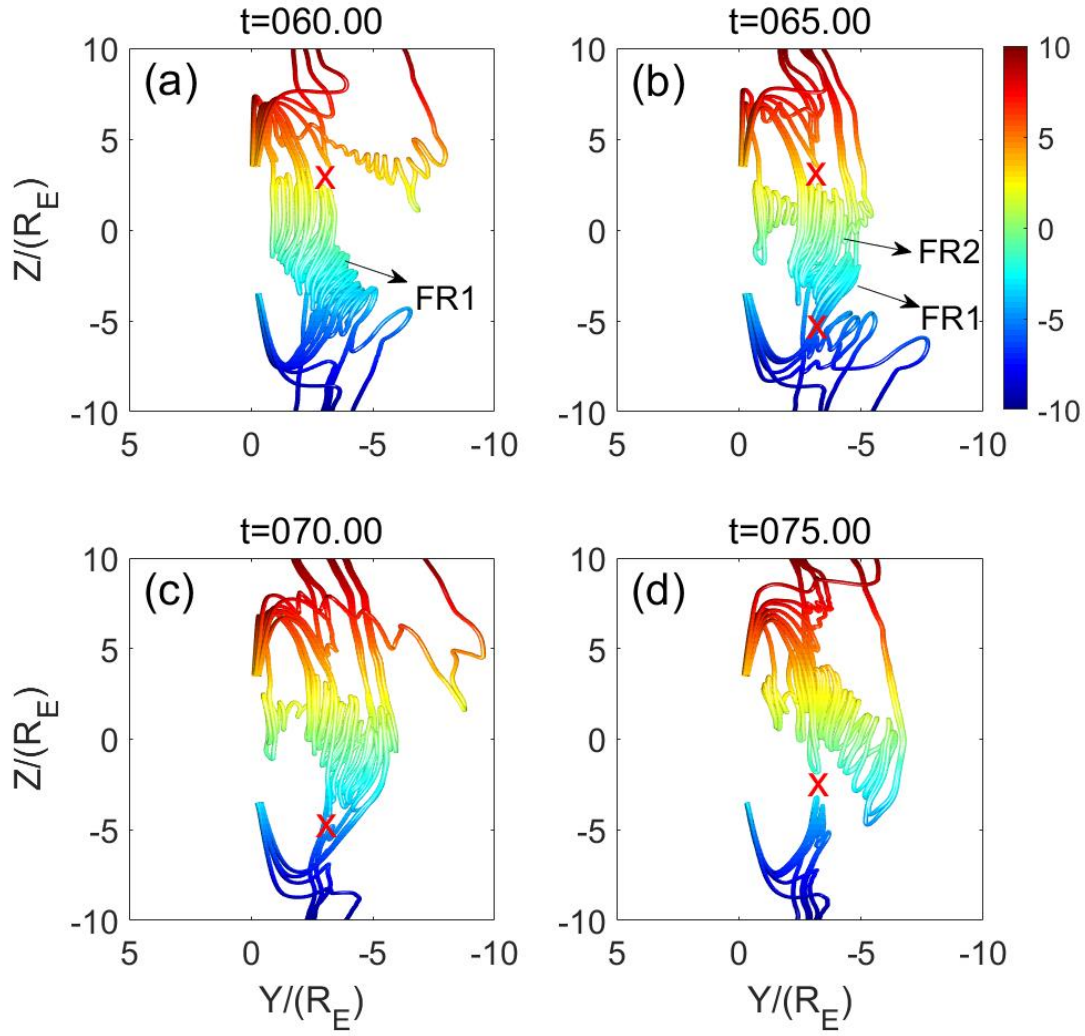

Figure 8. Magnetic field line configuration in 3-D perspective around the Y=-3.2 plane in case 1 at t=60 (a), 65 (b), 70 (c), and 75 (d). The field lines are color-coded according to their Z coordinates. The red mark 'X' represents the position of the X-line in the Y=-3.2 plane.

To better understand the 3-D coalescence process, we draw the time evolution of 3-D magnetic field line configuration around the Y=-3.2 plane in Figure 8. At t=60, the southward-moving FR1 is wrapped by

575 northward-moving reconnected magnetic field lines in regions with
576 Y>-3.2. In the Y=-3.2 plane, only one reconnection X-point exists at
577 Z=+2 (Figure 8a). At t=65, FR2 is generated on the northern side of FR1,
578 and new reconnection occurs at Z=-5 (Figure 8b). Both FR1 and FR2 are
579 wrapped together by the northward-moving reconnected magnetic field
580 lines (Figure 7b and Figure 8b), which indicates that the coalescence is
581 driven by the northward reconnection outflow of the new reconnection at
582 Z=-5. At t=70, this coalescence is also present in the extended regions in
583 the -Y direction and pulls the southward-moving FR1 northward to merge
584 with FR2 (Figures 8b-8d). Reconnection around the X-point at Z=+2 is
585 inhibited by the northward reconnection outflow and disappears (Figures
586 7c and 8c). At t=75, the coalescence between FR1 and FR2 is completed,
587 and the two FRs are replaced by a new FR with a larger diameter (Figure
588 8d). The axis of the new FR is tilted in the Z direction due to the spatial
589 variation of convection velocity at different Y locations and the guide
590 field B_y. Our results agree with the previous global hybrid simulation by
591 Guo et al (2020), which shows the tilted FRs due to the presence of guide
592 field. Therefore, a coalescence that begins at a nearby coordinate Y and
593 the associated convection of field lines can affect the motion and
594 interaction of FRs, which then further affects the reconnection locations.
595 The tilted FRs, which have also been observed at the magnetopause (Teh
596 et al., 2017) and in the magnetotail (Teh et al., 2018; Man et al., 2020;

Jiang et al., 2023), as well as the spreading of their coalescence in the Y direction, however, cannot be revealed by 2-D models.

5.2 Reconnection inside FRs

It is also found in our simulation that reconnection can take place inside FRs, which also affects the variation of reconnection locations. Figure 9 shows the contours of V_{pz} and 2-D view of magnetic field line configuration during the evolution of reconnection inside FR3 in case 1. As shown inside the red ellipse in Figure 9a (t=135), the length scale of FR3 can be ~10 R_E in the Z direction, extending across the equator. The V_{pz} reversal locations on the northern and southern sides of FR3 are no longer at the X-points of the projected field but rather inside FR3. The magnetopause flow velocity is ~1 V_{A0} at the X-line northward of FR3 and ~-0.6 V_{A0} at the X-line southward of FR3, comparable with but somewhat smaller than the average magnetosheath flow speed of ~1 V_{A0}. FR3 and the magnetopause current sheet around it are stretched by the northward flow in the northern hemisphere and southward flow in the southern hemisphere. As a result, new reconnection is triggered in the current sheet (Figures 9a-9c). At t=140, FR3 is splitting into two FRs (FR4 and FR5). The reconnection locations shift to the center of FR3 (Figure 9b).

Figures 9d-9e show the line cuts of the B_x component and the flow component V_{pz}, respectively, along the magnetopause surface in the

619 noon-median (Y=0) plane at t=140. In these line cuts, reconnection
620 location is identified by the B_x reversal from positive to negative and the
621 bulk velocity component V_{pz} reversal from negative to positive at Z=-1.
622 At t=145, FR3 has fully split into FR4, FR5, and a small FR (FR6). FR6
623 is generated by the secondary reconnection under a strong northward flow
624 inside FR3 at Z=+3. The flow component V_{pz} in the magnetopause is
625 larger than that in the magnetosheath, as seen from the darker colors
626 inside FR4 and FR5, and the flow reversal is located at the X-type
627 magnetic configuration (Z=-1). The splitting of a large-scale FR into two
628 smaller FRs has recently been observed at the Earth's magnetopause
629 (Zhong et al., 2023). In general, multiple X-line reconnection can be
630 affected by the strong northward or southward magnetosheath flows
631 before the reconnection inside FR3 has fully developed (i.e. before the
632 FR3 separates into two FRs). Ions are accelerated by the new
633 reconnection inside FR3, and then reconnection on the north and south
634 sides of FR3 is found to be inhibited by the new reconnection outflow.

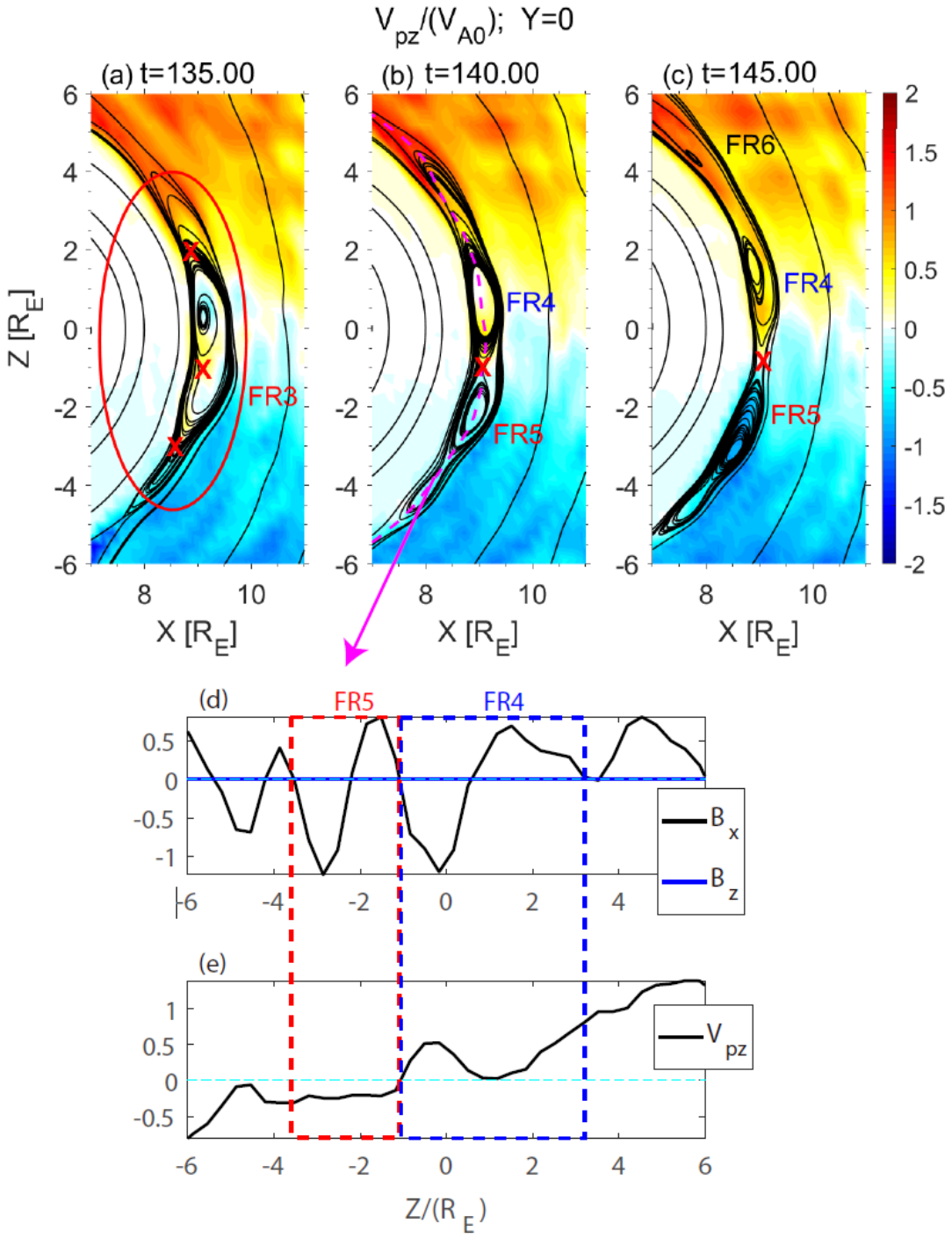

635

636 Figure 9. Evolution of reconnection inside FR3 in case 1. Contours of ion
637 bulk velocity component V_{pz} at t=135 (a), t=140 (b), and t=145 (c); line
638 cuts of magnetic field component B_x and B_z (d), and ion bulk velocity
639 component V_{pz} (e) along the magnetopause surface in the noon-median
640 (Y=0) plane at t=140. The red mark 'X' indicates the location of ion flow

reversal from negative to positive. The red and blue dashed boxes in Figures 9d-7e represent the flux ropes FR5 and FR4, respectively.

The 3-D magnetic field line configuration around the noon-meridian plane is also provided in Figure 10. At t=130, the flux rope FR3 extending in the Y and Z directions (predominantly in Z) is located between Z>-5 and Z<+5 (Figure 10a). At t=135, FR3 stretches in the $\pm$Z direction (Figure 10b). At t=140, reconnection inside FR3 is triggered, and three new FRs (FR4, FR5, and FR6) are separated from FR3 (Figure 10c). FR4 and FR5 are generated by reconnection with V_{pz} reversal at the Z=-1. FR6 is generated by secondary reconnection at Z=+3. It is worth noting that the features of FR6 do not appear in the 2-D view in Figure 9b and the line cuts of the magnetic field in Figure 9d (t=140), because the axial direction of FR6 is mainly in the Z direction. The effects of secondary reconnection on the global distribution of magnetopause reconnection are beyond the scope of this paper. At t=145, the new reconnection outflow transports FRs from the low-latitude region toward the high-latitude region. The distance between FR4 and FR5 becomes larger than that at t=140, as FR4 propagates northward and FR5 is transported southward. Overall, the location of reconnection has shifted to Z=-1 due to reconnection inside FR3.

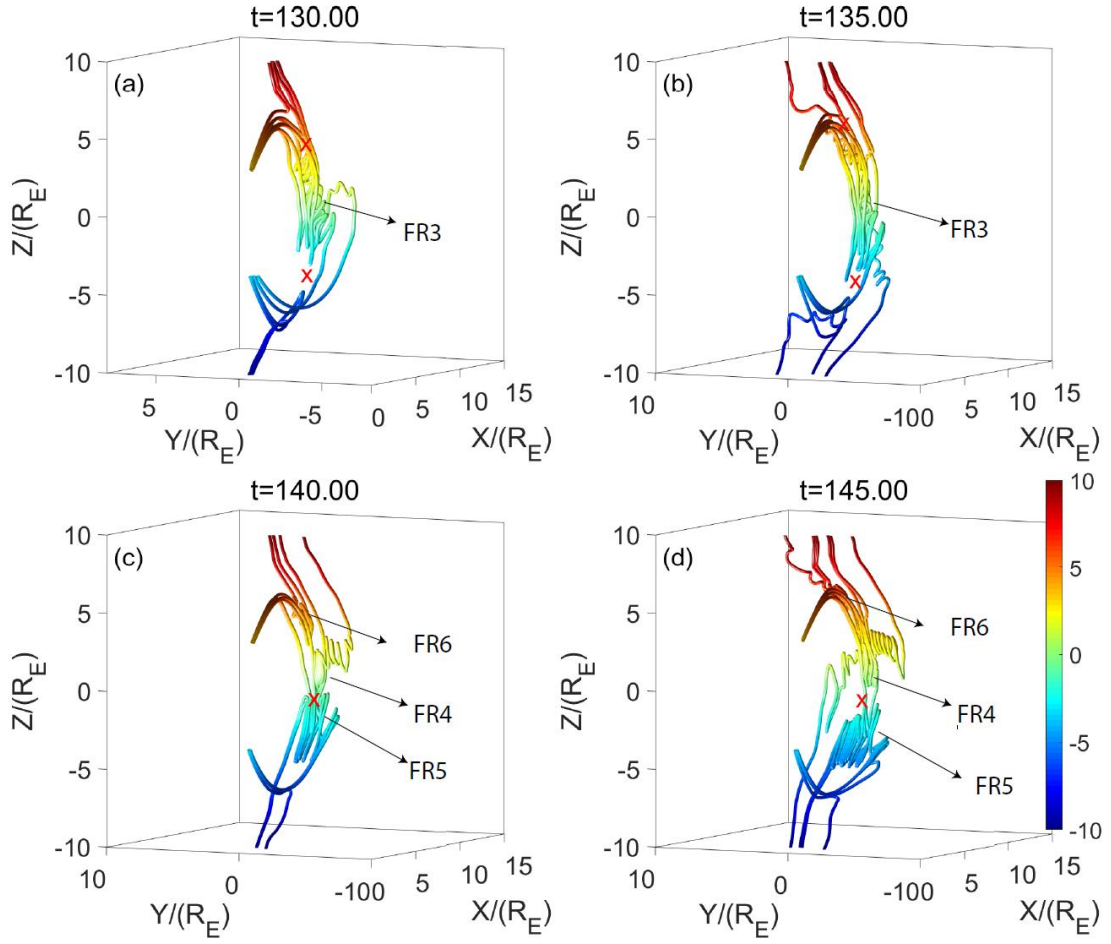

Figure 10. 3-D magnetic field line configurations around the noon-meridian plane in case 1, at t=130 (a), t=135 (b), t=140 (c), and t=145 (d). The field lines are color-coded according to their Z coordinate. The red mark 'X' represents the position of the X-point in the noon-meridian plane.

5.3 Reconnection near the equator and effects of magnetosheath flow

Under the southward IMF conditions with finite IMF B_x, reconnection first occurs in a high-latitude region (Figures 4a and 5a) downstream of the quasi-perpendicular shock, consistent with the anti-parallel

673 reconnection scenario. Then, in the middle stage of the simulation,
674 subsolar reconnection between the northward geomagnetic field and the
675 southward IMF is found to have developed and become steadier than
676 reconnection in the high-latitude region. The reason for the formation of
677 the steadier low-latitude reconnection is that the strong northward or
678 southward magnetosheath flow in the high-latitude region induces the
679 sliding motion of the X-line along the magnetopause (Tanaka et al., 2010).
680 Then the high-latitude reconnection near the noon-meridian plane is
681 suppressed by the subsolar reconnection outflow and eventually
682 dominated by the low-latitude reconnection (Figures 4c and 5b). As the
683 magnetopause current sheet is further stretched by the magnetosheath
684 flow, low-latitude reconnection is also triggered on the dawn and dusk
685 sides.

686 Figure 11 depicts the contours of ion velocity component V_{pz} in the
687 Y=-8.6 plane (dawn side) superposed with the nearby 3-D magnetic field
688 lines in case 2 with a negative IMF B_x. At t=60, a V_{pz} reversal at the
689 magnetopause and the reconnection X-lines are located at Z=-3.2 (Figure
690 11a). The average $|V_{pz}|$ ($\sim 1.3V_{A0}$) of the magnetosheath flow is
691 comparable to and somewhat larger than the magnetopause $|V_{pz}|$ ($\sim 1V_{A0}$)
692 near Z=-3.2. The V_{pz} flow reversal in the magnetosheath is located at
693 Z=+2, signifying that the magnetopause reconnection X-line at Z=-3.2 is
694 situated against the backdrop of a southward magnetosheath flow. At t=70,

new reconnection occurs in the low-latitude region near Z=+2 where the magnetopause flow reversal at this position coincides with magnetosheath flow reversal (Figure 11b). At t=80, a new FR is generated in Y>-8.6 (Figure 11c, duskward of the contour plane). In Y<=-8.6, on the other hand, the magnetopause reconnection in the southern hemisphere is inhibited by the southward magnetosheath flow. At t=100, the locations of magnetopause reconnection in the Y<=-8.6 planes are dominated by those near the equator (Figure 11d). Besides, it is worth noting that reconnection locations at Z=-3.2 still exist in the Y>-8.6 planes, where multiple X-line reconnection is also in process. After the reconnection locations shift to the vicinity of the equator, they tend to remain quasi-steady in the low-latitude regions, with slight position changes caused by the generation, transport, and coalescence of the FRs.

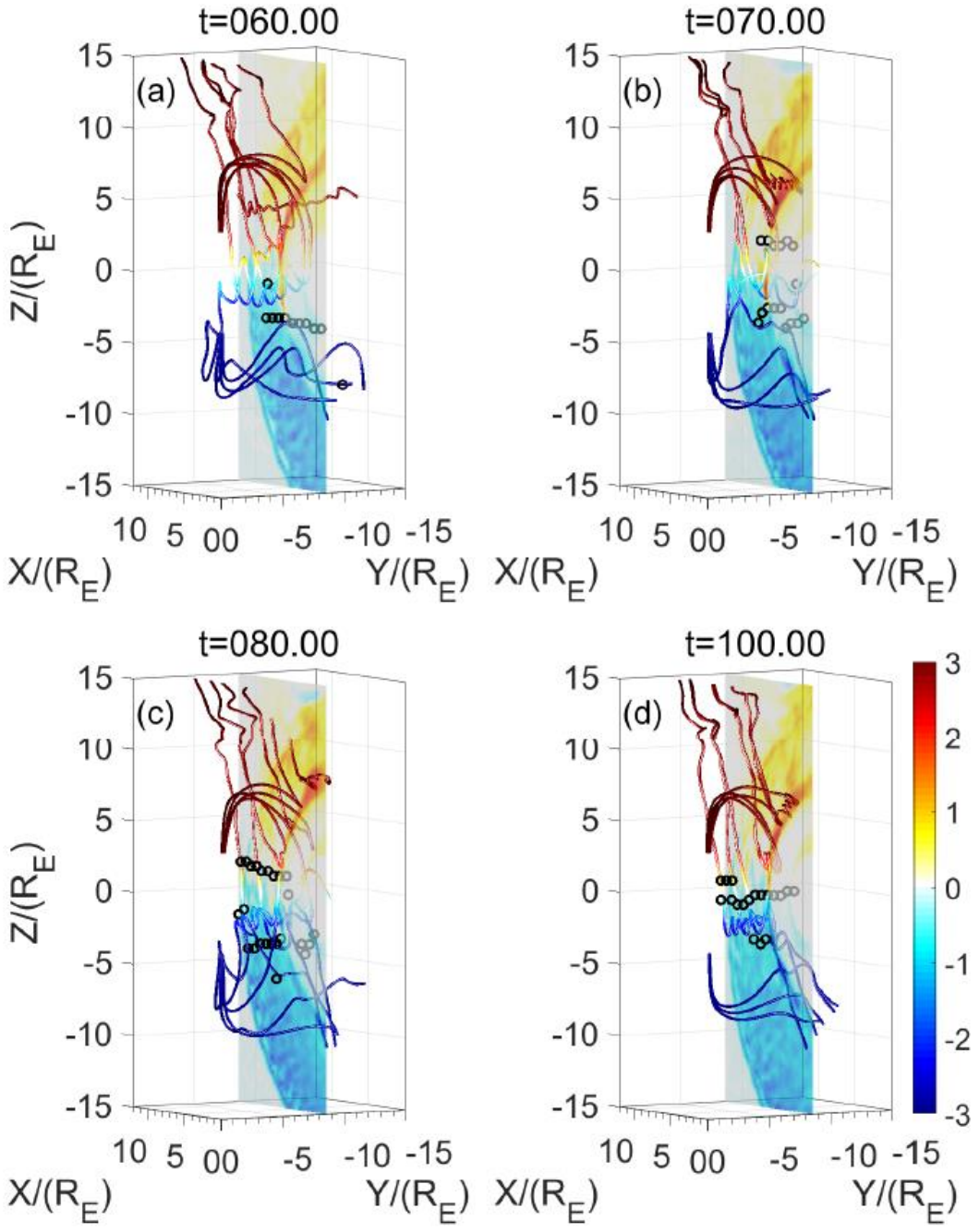

Figure 11. Contours of ion flow component V_{pz} in the Y=-8.6 plane together with 3-D magnetic field lines in case 2 at various times. The black circles represent the magnetopause reconnection locations.

6. Summary

In this paper, we have studied the dynamic evolution of dayside

magnetopause reconnection locations and their dependence on the IMF cone angle via 3-D global hybrid simulations. The main conclusions are as follows.

1. Under purely southward IMF conditions, reconnection begins from around the equator, and the reconnection sites exhibit a dynamic evolution that extends beyond the equatorial region. The X-lines are not always parallel to the equatorial plane, even though the IMF is southward. Our results demonstrate detailed manners of the evolution of global reconnection structures, including tilted FRs, tilted reconnection lines, and the spreading of FR coalescence in the Y direction. Nevertheless, these highly dynamic reconnection locations tend to shift to the equator and maintain quasi-steady in the low-latitude regions in the later stage of simulation.
2. In the presence of a finite IMF B_x, reconnection initially occurs in the high-latitude regions downstream of the quasi-perpendicular bow shock, where the magnetic field lines are antiparallel. Similar to the case with a purely southward IMF, the magnetopause reconnection evolves dynamically under steady upstream conditions. Eventually, the magnetopause is dominated by low-latitude reconnection, while reconnection in the high-latitude regions is inhibited by the outflow of the low-latitude reconnection as well as the magnetosheath flow. The average locations of reconnection maintain quasi-steady in the

low-latitude regions, regardless of the sign of IMF B_x.

3. The presence of IMF B_x controls the location of reconnection by affecting the thickness of the magnetopause current sheet. In the early stage of simulation, reconnection occurs in high-latitude (θ_{shear}~180°, quasi-perpendicular shock) where the magnetopause current sheet is the thinnest. The current sheet is thicker in other regions with smaller θ_{shear}. Such occurrence of reconnection in the region characterized by antiparallel magnetic field lines supports the views of Dungey (1961, 1963), Luhmann et al. (1984), and Trattner et al. (2005, 2007). Nevertheless, a relatively thin local magnetopause current sheet is found to also develop in the extended areas over the dayside magnetopause, where the shocked magnetosheath field lines are compressed by the solar wind (Kivelson & Russell, 1995; Lopez et al., 2017; Madelaire et al., 2022). Since the shocked IMF lines are highly curved, large θ_{shear} exists in broad regions. Subsequently, reconnection can occur over a large range of the dayside magnetopause. Therefore, reconnection locations are no longer controlled by the initial IMF conditions in the dynamic magnetopause. We have examined other cases with different IMF cone angles (not shown in this paper) and obtained similar results.
4. Predominant magnetopause reconnection can be effectively identified by the locations of B_x reversal and the reversal of the ion flow velocity

component V_{pz} on the magnetopause surface. It is worth noting that the X-lines identified with simultaneous B_x and V_{pz} reversals tend to possess quasi-steady reconnection locations, while X-lines without V_{pz} reversal tend to be transient as they are easily carried away by significant poleward background flows in higher latitudes.

5. Overall, we find that dayside magnetopause reconnection locations not only depend on the initial IMF directions but also the local dynamic processes of the magnetopause, e.g., the generation, coalescence, and transportation of FRs, reconnection inside the FRs, low-latitude reconnection, and magnetosheath flow.

Previous observations (Zou et al., 2022) and simulations (Hoilijoki et al., 2017, 2019; Pfau-Kempf et al., 2020) suggested that perturbations in the magnetosheath driven by foreshock waves can modulate the magnetopause reconnection. Chen et al. (2021) showed that the magnetosheath fluctuations can induce magnetopause reconnection. However, recent observational statistics obtained by Petrinec et al. (2022) showed that enhanced magnetosheath fluctuations are unlikely to trigger magnetic reconnection at random magnetopause locations. Such results indicate that increased fluctuations do not enhance the occurrence of steady magnetic reconnection at the magnetopause. Our present study focuses on the predominant and primary reconnection locations, for which we do not see the significant effects of foreshock waves.

A particular aspect of our study is the investigation of the relation between magnetic shear angle and the magnetopause reconnection under finite IMF B_x and B_z. In the existing Maximum Shear Model, an empirical approach is employed to predict the location of reconnection X-lines on the magnetopause surface based on the maximum magnetic shear angle (Trattner et al., 2007). Since its introduction, various studies in the literature have assessed the performance of the Maximum Shear Model. It is found that the Maximum Shear Model would not lose statistical accuracy when the IMF is dominated by a southward IMF B_z (Trattner et al., 2007; Qudsi et al., 2023) or IMF B_y (Trattner et al., 2017). However, for large $|B_x|/|B|$, the model predicts only antiparallel reconnection due to inaccuracies in modeling the magnetosheath field line draping (Trattner et al., 2007). Fuselier et al. (2017) noted that the Maximum Shear Model struggles to predict reconnection location under some conditions, such as vortex structures of the KH waves and IMF B_x dominant X-line events with a strong guide field. In this study, we find that the maximum shear angle model exhibits good performance in the case with purely southward conditions, consistent with the IMF-B_z dominant observations (Trattner et al., 2007; Qudsi et al., 2023). In the case with IMF B_x, the maximum shear angle model exhibits accurate predictions in the early stage of global reconnection, when the thinnest current sheet exists downstream of quasi-perpendicular shocks where the

field is antiparallel, leading to reconnection in this high-latitude boundary layer. Nevertheless, due to the magnetosheath field lines draping around the magnetopause, almost entire magnetopause displays large shear angles except on the dawn and dusk sides. In the later stage, reconnection is not confined to the region with maximum shear angle.

Acknowledge

This work was supported by the National Natural Science Foundation of China (NSFC) under Grant Nos. 42130211, 41774154, and 42074197, and the National Science Foundation grant NSF-OIA-2148652. The PIC simulations were performed by using the TH-2 supercomputer at the National Supercomputing Center in Guangzhou (NSCC-GZ) and the supercomputer at Nanchang University. We also thank Nanchang University and Auburn University for the academic exchange opportunity to complete this work.

Data Availability Statement

The simulation data used in this study are available at https://doi.org/10.17605/OSF.IO/D7B56

Reference

Akasofu, S. I. (1981). Energy coupling between the solar wind and the

magnetosphere. Space Science Reviews, 28, 121-190. https://doi.org/10.1007/BF00218810

Anekallu, C. R., Palmroth, M., J. Koskinen, H. E., Lucek, E., & Dandouras, I. (2013). Spatial variation of energy conversion at the Earth's magnetopause: Statistics from Cluster observations. Journal of Geophysical Research: Space Physics, 118(5), 1948-1959. https://doi.org/10.1002/jgra.50233

Burch, J. L., & Phan, T. D. (2016). Magnetic reconnection at the dayside magnetopause: Advances with MMS. Geophysical Research Letters, 43(16), 8327-8338. https://doi.org/10.1002/2016GL069787

Burch, J. L., Moore, T. E., Torbert, R. B., & Giles, B. H. (2016). Magnetospheric multiscale overview and science objectives. Space Science Reviews, 199, 5-21. https://doi.org/10.1007/s11214-015-0164-9

Chen, L. J., Ng, J., Omelchenko, Y., & Wang, S. (2021). Magnetopause reconnection and indents induced by foreshock turbulence. Geophysical Research Letters, 48(11), e2021GL093029. https://doi.org/10.1029/2021GL093029

Cnossen, I., Wiltberger, M., & Ouellette, J. E. (2012). The effects of seasonal and diurnal variations in the Earth's magnetic dipole orientation on solar wind–magnetosphere-ionosphere coupling. Journal of Geophysical Research: Space Physics, 117(A11).

https://doi.org/10.1029/2012JA017825

Dai, J. G., Wang, C. S., Liu, S. A., Qian, X. Y., Zhu, D. C., & Ke, S. (2016). Deep carbon cycle recorded by calcium-silicate rocks (rodingites) in a subduction-related ophiolite. Geophysical Research Letters, 43(22), 11-635. https://doi.org/10.1002/2016GL070474

Daughton, W., Scudder, J., & Karimabadi, H. (2006). Fully kinetic simulations of undriven magnetic reconnection with open boundary conditions. Physics of Plasmas, 13(7). https://doi.org/10.1063/1.2218817

Dong, X. C., Dunlop, M. W., Wang, T. Y., Trattner, K. J., Russell, C. T., & Giles, B. (2020). MMS observation of secondary magnetic reconnection beside ion-scale flux rope at the magnetopause. Geophysical Research Letters, 47(16), e2020GL089075. https://doi.org/10.1029/2020GL089075

Dungey, J. W. (1961). Interplanetary magnetic field and the auroral zones. Physical Review Letters, 6(2), 47. https://doi.org/10.1103/PhysRevLett.6.47

Dungey, J. W., Geophysics, The Earth's Environment DeWitt, Hieblot, Lebeau, 503, Gordon and Breach, New York, N. Y., 1963.

Fear, R. C., Milan, S. E., Fazakerley, A. N., Owen, C. J., Asikainen, T., Taylor, M. G. G. T., ... & Daly, P. W. (2007, July). Motion of flux transfer events: A test of the Cooling model. In Annales Geophysicae

(Vol. 25, No. 7, pp. 1669-1690). Göttingen, Germany: Copernicus Publications. https://doi.org/10.5194/angeo-25-1669-2007

Fear, R. C., Palmroth, M., & Milan, S. E. (2012). Seasonal and clock angle control of the location of flux transfer event signatures at the magnetopause. Journal of Geophysical Research: Space Physics, 117(A4). https://doi.org/10.1029/2011JA017235

Fu, H. S., Peng, F. Z., Liu, C. M., Burch, J. L., Gershman, D. G., & Le Contel, O. (2019). Evidence of electron acceleration at a reconnecting magnetopause. Geophysical Research Letters, 46(11), 5645-5652. https://doi.org/10.1029/2019GL083032

Fuselier, S. A., Vines, S. K., Burch, J. L., Petrinec, S. M., Trattner, K. J., Cassak, P. A., ... & Webster, J. M. (2017). Large-scale characteristics of reconnection diffusion regions and associated magnetopause crossings observed by MMS. Journal of Geophysical Research: Space Physics, 122(5), 5466-5486. https://doi.org/10.1002/2017JA024024

Guo, J., Lu, S., Lu, Q., Lin, Y., Wang, X., Huang, K., ... & Wang, S. (2021). Re-reconnection processes of magnetopause flux ropes: Three-dimensional global hybrid simulations. Journal of Geophysical Research: Space Physics, 126(6), e2021JA029388. https://doi.org/10.1029/2021JA029388

Guo, J., Lu, S., Lu, Q., Lin, Y., Wang, X., Zhang, Q., ... & Wang, S. (2021). Three-Dimensional Global Hybrid Simulations of High

Latitude Magnetopause Reconnection and Flux Ropes During the Northward IMF. Geophysical Research Letters, 48(21), e2021GL095003. https://doi.org/10.1029/2021GL095003

Guo, J., Lu, S., Lu, Q., Lin, Y., Wang, X., Huang, K., ... & Wang, S. (2021). Structure and coalescence of magnetopause flux ropes and their dependence on IMF clock angle: Three-dimensional global hybrid simulations. Journal of Geophysical Research: Space Physics, 126(2), e2020JA028670. https://doi.org/10.1029/2020JA028670

Guo, Z., Lin, Y., Wang, X., Vines, S. K., Lee, S. H., & Chen, Y. (2020). Magnetopause reconnection as influenced by the dipole tilt under southward IMF conditions: Hybrid simulation and MMS observation. Journal of Geophysical Research: Space Physics, 125(9), e2020JA027795. https://doi.org/10.1029/2020JA027795

Guo, Z., Lin, Y., & Wang, X. (2021). Global hybrid simulations of interaction between interplanetary rotational discontinuity and bow shock/magnetosphere: Can ion-scale magnetic reconnection be driven by rotational discontinuity downstream of quasi-parallel shock?. Journal of Geophysical Research: Space Physics, 126(4), e2020JA028853. https://doi.org/10.1029/2020JA028853

Hoilijoki, S., Souza, V. M., Walsh, B. M., Janhunen, P., & Palmroth, M. (2014). Magnetopause reconnection and energy conversion as influenced by the dipole tilt and the IMF Bx. Journal of Geophysical

913 Research: Space Physics, 119(6), 4484-4494.
914 https://doi.org/10.1002/2013JA019693
915 Hoilijoki, S., Ganse, U., Pfau-Kempf, Y., Cassak, P. A., Walsh, B. M.,
916 Hietala, H., ... & Palmroth, M. (2017). Reconnection rates and X line
917 motion at the magnetopause: Global 2D-3V hybrid-Vlasov simulation
918 results. Journal of Geophysical Research: Space Physics, 122(3),
919 2877-2888. https://doi.org/10.1002/2016JA023709.
920 Hoilijoki, S., Ganse, U., Sibeck, D. G., Cassak, P. A., Turc, L., Battarbee,
921 M., ... & Palmroth, M. (2019). Properties of magnetic reconnection and
922 FTEs on the dayside magnetopause with and without positive IMF B x
923 component during southward IMF. Journal of Geophysical Research:
924 Space Physics, 124(6), 4037-4048.
925 https://doi.org/10.1029/2019JA026821
926 Hoppe, M. M., & Russell, C. T. (1983). Plasma rest frame frequencies
927 and polarizations of the low-frequency upstream waves: ISEE 1 and 2
928 observations. Journal of Geophysical Research: Space Physics, 88(A3),
929 2021-2027. https://doi.org/10.1029/ja088ia03p02021
930 Huang, S. Y., Sahraoui, F., Yuan, Z. G., He, J. S., Zhao, J. S., Le Contel,
931 O., ... & Burch, J. L. (2017). Magnetospheric multiscale observations
932 of electron vortex magnetic hole in the turbulent magnetosheath
933 plasma. The Astrophysical Journal Letters, 836(2), L27.
934 https://doi.org/10.3847/2041-8213/aa5f50

935 Kawano, H., & Russell, C. T. (1997). Survey of flux transfer events
936 observed with the ISEE 1 spacecraft: Dependence on the interplanetary
937 magnetic field. Journal of Geophysical Research: Space Physics,
938 102(A6), 11307-11313. https://doi.org/10.1029/97JA00481
939 Kitamura, N., Hasegawa, H., Saito, Y., Shinohara, I., Yokota, S., Nagai,
940 T., ... & Burch, J. L. (2016). Shift of the magnetopause reconnection
941 line to the winter hemisphere under southward IMF conditions: Geotail
942 and MMS observations. Geophysical Research Letters, 43(11),
943 5581-5588. https://doi.org/10.1002/2016GL069095.
944 Kivelson, M. G., & Russell, C. T. (Eds.). (1995). Introduction to space
945 physics. Cambridge university press.
946 Komar, C. M., Fermo, R. L., & Cassak, P. A. (2015). Comparative
947 analysis of dayside magnetic reconnection models in global
948 magnetosphere simulations. Journal of Geophysical Research: Space
949 Physics, 120(1), 276-294. https://doi.org/10.1002/2014JA020587
950 Laitinen, T. V., Palmroth, M., Pulkkinen, T. I., Janhunen, P., & Koskinen,
951 H. E. (2007). Continuous reconnection line and pressure-dependent
952 energy conversion on the magnetopause in a global MHD model.
953 Journal of Geophysical Research: Space Physics, 112(A11).
954 https://doi.org/10.1029/2007JA012352
955 Li, H., Jiang, W., Wang, C., Verscharen, D., Zeng, C., Russell, C. T., ... &
956 Burch, J. L. (2020). Evolution of the Earth’s magnetosheath turbulence:

957 A statistical study based on MMS observations. The Astrophysical
958 Journal Letters, 898(2), L43.
959 https://doi.org/10.3847/2041-8213/aba531
960 Lin, Y., & Wang, X. Y. (2005). Three-dimensional global hybrid
961 simulation of dayside dynamics associated with the quasi-parallel bow
962 shock. Journal of Geophysical Research: Space Physics, 110(A12).
963 https://doi.org/10.1029/2005JA011243
964 Lin, Y., & Wang, X. Y. (2006). Formation of dayside low-latitude
965 boundary layer under northward interplanetary magnetic field.
966 Geophysical research letters, 33(21).
967 https://doi.org/10.1029/2006GL027736
968 Lin, Y., Wang, X. Y., & Chang, S. W. (2007). Connection between bow
969 shock and cusp energetic ions. Geophysical research letters, 34(11).
970 https://doi.org/10.1029/2007GL030038
971 Liu, T. Z., Hietala, H., Angelopoulos, V., Omelchenko, Y., Roytershteyn,
972 V., & Vainio, R. (2019). THEMIS observations of particle acceleration
973 by a magnetosheath jet-driven bow wave. Geophysical Research
974 Letters, 46(14), 7929-7936. https://doi.org/10.1029/2019gl082614
975 Lopez, R. E., & Gonzalez, W. D. (2017). Magnetospheric balance of solar
976 wind dynamic pressure. Geophysical Research Letters, 44(7),
977 2991-2999. https://doi.org/10.1002/2017GL072817
978 Lyon, J. G. (2000). The solar wind-magnetosphere-ionosphere system.

Science, 288(5473), 1987-1991. https://doi.org/10.1126/science.288.5473.1987

Lu, J. Y., Liu, Z. Q., Kabin, K., Zhao, M. X., Liu, D. D., Zhou, Q., & Xiao, Y. (2011). Three dimensional shape of the magnetopause: Global MHD results. Journal of Geophysical Research: Space Physics, 116(A9). https://doi.org/10.1029/2010JA016418

Lu, J. Y., Jing, H., Liu, Z. Q., Kabin, K., & Jiang, Y. (2013). Energy transfer across the magnetopause for northward and southward interplanetary magnetic fields. Journal of Geophysical Research: Space Physics, 118(5), 2021-2033. https://doi.org/10.1002/jgra.50093

Lu, J. Y., Zhang, H. X., Wang, M., Kabin, K., Zhou, Y., & Li, J. Y. (2021). Energy transfer across the magnetopause under radial IMF conditions. The Astrophysical Journal, 920(1), 52. https://doi.org/10.3847/1538-4357/ac15f4

Luhmann, J. G., Walker, R. J., Russell, C. T., Crooker, N. U., Spreiter, J. R., & Stahara, S. S. (1984). Patterns of potential magnetic field merging sites on the dayside magnetopause. Journal of Geophysical Research: Space Physics, 89(A3), 1739-1742. https://doi.org/10.1029/JA089iA03p01739

Jiang, K., Huang, S. Y., Yuan, Z. G., Xiong, Q. Y., & Wei, Y. Y. (2023). Observations of tilted electron vortex flux rope in the magnetic reconnection tailward outflow region. Geophysical Research Letters,

50(17), e2023GL105006. https://doi.org/10.1029/2023GL105006

Man, H. Y., Zhou, M., Yi, Y. Y., Zhong, Z. H., Tian, A. M., Deng, X. H., ... & Giles, B. L. (2020). Observations of electron-only magnetic reconnection associated with macroscopic magnetic flux ropes. Geophysical Research Letters, 47(19), e2020GL089659. https://doi.org/10.1029/2020GL089659

Madelaire, M., Laundal, K. M., Reistad, J. P., Hatch, S. M., Ohma, A., & Haaland, S. (2022). Geomagnetic Response to Rapid Increases in Solar Wind Dynamic Pressure: Event Detection and Large Scale Response. Frontiers in Astronomy and Space Sciences, 9, 904620. https://doi.org/10.3389/fspas.2022.904620

Mozer, F. S., Pritchett, P. L., Bonnell, J., Sundkvist, D., & Chang, M. T. (2008). Observations and simulations of asymmetric magnetic field reconnection. Journal of Geophysical Research: Space Physics, 113(A1). https://doi.org/10.1029/2008JA013535

Omidi, N., Blanco-Cano, X., Russell, C. T., & Karimabadi, H. (2006). Global hybrid simulations of solar wind interaction with Mercury: Magnetosperic boundaries. Advances in Space Research, 38(4), 632-638. https://doi.org/10.1016/j.asr.2005.11.019

Omidi, N., & Sibeck, D. G. (2007). Flux transfer events in the cusp. Geophysical Research Letters, 34(4). https://doi.org/10.1029/2006GL028698

Paschmann, G. (1997). Observational evidence for transfer of plasma across the magnetopause. In Transport Across the Boundaries of the Magnetosphere: Proceedings of an ISSI Workshop October 1–5, 1996, Bern, Switzerland (pp. 217-234). Springer Netherlands. https://doi.org/10.1023/A:1004926004806

Palmroth, M., Pulkkinen, T. I., Janhunen, P., & Wu, C. C. (2003). Stormtime energy transfer in global MHD simulation. Journal of Geophysical Research: Space Physics, 108(A1). https://doi.org/10.1029/2002JA009446

Palmroth, M., Laitinen, T. V., & Pulkkinen, T. I. (2006, December). Magnetopause energy and mass transfer: results from a global MHD simulation. In Annales geophysicae (Vol. 24, No. 12, pp. 3467-3480). Göttingen, Germany: Copernicus Publications. https://doi.org/10.5194/angeo-24-3467-2006

Pang, Y., Lin, Y., Deng, X. H., Wang, X. Y., & Tan, B. (2010). Three-dimensional hybrid simulation of magnetosheath reconnection under northward and southward interplanetary magnetic field. Journal of Geophysical Research: Space Physics, 115(A3). https://doi.org/10.1029/2009JA014415

Park, K. S., Ogino, T., & Walker, R. J. (2006). On the importance of antiparallel reconnection when the dipole tilt and IMF By are nonzero. Journal of Geophysical Research: Space Physics, 111(A5).

https://doi.org/10.1029/2004JA010972

Peng, Z., Wang, C., & Hu, Y. Q. (2010). Role of IMF Bx in the solar wind-magnetosphere-ionosphere coupling. Journal of Geophysical Research: Space Physics, 115(A8). https://doi.org/10.1029/2010JA015454

Peng, F. Z., Fu, H. S., Cao, J. B., Graham, D. B., Chen, Z. Z., Cao, D., ... & Burch, J. L. (2017). Quadrupolar pattern of the asymmetric guide-field reconnection. Journal of geophysical research: Space physics, 122(6), 6349-6356. https://doi.org/10.1002/2016JA023666

Petrinec, S. M., Burch, J. L., Fuselier, S. A., Trattner, K. J., Giles, B. L., & Strangeway, R. J. (2022). On the occurrence of magnetic reconnection along the terrestrial magnetopause, using Magnetospheric Multiscale (MMS) observations in proximity to the reconnection site. Journal of Geophysical Research: Space Physics, 127(6), e2021JA029669. https://doi.org/10.1029/2021JA029669

Pfau-Kempf, Y., Palmroth, M., Johlander, A., Turc, L., Alho, M., Battarbee, M., ... & Ganse, U. (2020). Hybrid-Vlasov modeling of three-dimensional dayside magnetopause reconnection. Physics of Plasmas, 27(9). https://doi.org/10.1063/5.0020685

Phan, T. D., Dunlop, M. W., Paschmann, G., Klecker, B., Bosqued, J. M., Reme, H., ... & Kistler, L. M. (2004, July). Cluster observations of continuous reconnection at the magnetopause under steady

interplanetary magnetic field conditions. In Annales Geophysicae (Vol. 22, No. 7, pp. 2355-2367). Copernicus GmbH. https://doi.org/10.5194/angeo-22-2355-2004, 2004

Pi, G., Němeček, Z., Šafránková, J., Grygorov, K., & Shue, J. H. (2018). Formation of the dayside magnetopause and its boundary layers under the radial IMF. Journal of Geophysical Research: Space Physics, 123(5), 3533-3547. https://doi.org/10.1029/2018JA025199

Pritchett, P. L. (2008). Collisionless magnetic reconnection in an asymmetric current sheet. Journal of Geophysical Research: Space Physics, 113(A6). https://doi.org/10.1029/2007JA012930

Pritchard, K. R., Burch, J. L., Fuselier, S. A., Webster, J. M., Torbert, R. B., Argall, M. R., ... & Strangeway, R. J. (2019). Energy conversion and electron acceleration in the magnetopause reconnection diffusion region. Geophysical Research Letters, 46(17-18), 10274-10282. https://doi.org/10.1029/2019GL084636

Qiu, H., Han, D. S., Wang, B., Feng, H., Li, B., Zhou, S., ... & Zhang, Y. L. (2022). In situ observation of a magnetopause indentation that is correspondent to throat aurora and is caused by magnetopause reconnection. Geophysical Research Letters, 49(15), e2022GL099408. https://doi.org/10.1029/2022GL099408

Qudsi, R. A., Walsh, B. M., Broll, J., Atz, E., & Haaland, S. (2023). Statistical Comparison of Various Dayside Magnetopause

Reconnection X-Line Prediction Models. Journal of Geophysical Research: Space Physics, 128(10), e2023JA031644. https://doi.org/10.1029/2023JA031644

Russell, C. T., & Elphic, R. C. (1978). Initial ISEE magnetometer results: Magnetopause observations. Space Science Reviews, 22, 681-715. https://doi.org/10.1007/BF00212619

Russell, C. T., & Hoppe, M. M. (1983). Upstream waves and particles. Space Science Reviews, 34(2), 155-172. https://doi.org/10.1007/978-94-009-7096-0_12

Russell, C. T., Wang, Y. L., & Raeder, J. (2003). Possible dipole tilt dependence of dayside magnetopause reconnection. Geophysical Research Letters, 30(18). https://doi.org/10.1029/2003GL017725

Scholer, M. (1990). Diffuse ions at a quasi-parallel collisionless shock: Simulations. Geophysical research letters, 17(11), 1821-1824. https://doi.org/10.1029/gl017i011p01821

Shay, M. A., Phan, T. D., Haggerty, C. C., Fujimoto, M., Drake, J. F., Malakit, K., ... & Swisdak, M. (2016). Kinetic signatures of the region surrounding the X line in asymmetric (magnetopause) reconnection. Geophysical Research Letters, 43(9), 4145-4154. https://doi.org/10.1002/2016GL069034

Shi, F., Cheng, L., Lin, Y., & Wang, X. (2017). Foreshock wave interaction with the magnetopause: Signatures of mode conversion.

Journal of Geophysical Research: Space Physics, 122(7), 7057-7076. https://doi.org/10.1002/2016ja023114

Shi, C., Zhao, J., Huang, J., Wang, T., Wu, D., Chen, Y., ... & Bale, S. D. (2021). Parker solar probe observations of Alfvénic waves and ion-cyclotron waves in a small-scale flux rope. The Astrophysical Journal Letters, 908(1), L19. https://doi.org/10.3847/2041-8213/abdd28

Swift, D. W. (1996). Use of a hybrid code for global-scale plasma simulation. Journal of Computational Physics, 126(1), 109-121. https://doi.org/10.1006/jcph.1996.0124

Tan, B., Lin, Y., Perez, J. D., & Wang, X. Y. (2011). Global-scale hybrid simulation of dayside magnetic reconnection under southward IMF: Structure and evolution of reconnection. Journal of Geophysical Research: Space Physics, 116(A2). https://doi.org/10.1029/2010JA015580

Tan, B., Lin, Y., Perez, J. D., & Wang, X. Y. (2012). Global-scale hybrid simulation of cusp precipitating ions associated with magnetopause reconnection under southward IMF. Journal of Geophysical Research: Space Physics, 117(A3). https://doi.org/10.1029/2011JA016871

Tanaka, K. G., Retinò, A., Asano, Y., Fujimoto, M., Shinohara, I., Vaivads, A., ... & Owen, C. J. (2008, August). Effects on magnetic reconnection of a density asymmetry across the current sheet. In Annales

Geophysicae (Vol. 26, No. 8, pp. 2471-2483). Göttingen, Germany: Copernicus Publications. https://doi.org/10.5194/angeo-26-2471-2008

Tanaka, K. G., Fujimoto, M., & Shinohara, I. (2010). Physics of magnetopause reconnection: A study of the combined effects of density asymmetry, velocity shear, and guide field. International Journal of Geophysics, 2010. https://doi.org/10.1155/2010/202583

Tang, B. B., Wang, C., & Li, W. Y. (2013). The magnetosphere under the radial interplanetary magnetic field: A numerical study. Journal of Geophysical Research: Space Physics, 118(12), 7674-7682. https://doi.org/10.1002/2013JA019155

Teh, W. L., Denton, R. E., Sonnerup, B. Ö., & Pollock, C. (2017). MMS observations of oblique small-scale magnetopause flux ropes near the ion diffusion region during weak guide-field reconnection. Geophysical Research Letters, 44(13), 6517-6524. https://doi.org/10.1002/2017GL074291

Trattner, K. J., Fuselier, S. A., Petrinec, S. M., Yeoman, T. K., Mouikis, C., Kucharek, H., & Reme, H. (2005). Reconnection sites of spatial cusp structures. Journal of Geophysical Research: Space Physics, 110(A4). https://doi.org/10.1029/2004JA010722

Trattner, K. J., Mulcock, J. S., Petrinec, S. M., & Fuselier, S. A. (2007). Location of the reconnection line at the magnetopause during southward IMF conditions. Geophysical Research Letters,

34(3):116-142. https://doi.org/10.1029/2006GL028397

Trattner, K. J., Petrinec, S. M., Fuselier, S. A., & Phan, T. D. (2012a). The location of reconnection at the magnetopause: Testing the maximum magnetic shear model with THEMIS observations. Journal of Geophysical Research: Space Physics, 117(A1). https://doi.org/10.1029/2011JA016959

Trattner, K. J., Petrinec, S. M., Fuselier, S. A., Omidi, N., & Sibeck, D. G. (2012b). Evidence of multiple reconnection lines at the magnetopause from cusp observations. Journal of Geophysical Research: Space Physics, 117(A1). https://doi.org/10.1029/2011JA017080

Trattner, K. J., Burch, J. L., Ergun, R., Fuselier, S. A., Gomez, R. G., Grimes, E. W., ... & Young, D. T. (2016). The response time of the magnetopause reconnection location to changes in the solar wind: MMS case study. Geophysical Research Letters, 43(10), 4673-4682. https://doi.org/10.1002/2016GL068554

Trattner, K. J., Burch, J. L., Ergun, R., Eriksson, S., Fuselier, S. A., Giles, B. L., ... & Wilder, F. D. (2017). The MMS dayside magnetic reconnection locations during phase 1 and their relation to the predictions of the maximum magnetic shear model. Journal of Geophysical Research: Space Physics, 122(12), 11-991. https://doi.org/10.1002/2017JA024488

Wang, B., Nishimura, Y., Hietala, H., Lyons, L., Angelopoulos, V.,

Plaschke, F., ... & Weatherwax, A. (2018). Impacts of magnetosheath high-speed jets on the magnetosphere and ionosphere measured by optical imaging and satellite observations. Journal of Geophysical Research: Space Physics, 123(6), 4879-4894. https://doi.org/10.1029/2017JA024954

Wang, H., Lin, Y., Wang, X., & Guo, Z. (2019). Generation of kinetic Alfvén waves in dayside magnetopause reconnection: A 3-D global-scale hybrid simulation. Physics of Plasmas, 26(7). https://doi.org/10.1063/1.5092561

Wang, T., Alexandrova, O., Perrone, D., Dunlop, M., Dong, X., Bingham, R., ... & Burch, J. L. (2019). Magnetospheric multiscale observation of kinetic signatures in the Alfvén vortex. The Astrophysical Journal Letters, 871(2), L22. https://doi.org/10.3847/2041-8213/aafe0d

Wang, R., Lu, Q., Nakamura, R., Baumjohann, W., Russell, C. T., Burch, J. L., ... & Gershman, D. (2017). Interaction of magnetic flux ropes via magnetic reconnection observed at the magnetopause. Journal of Geophysical Research: Space Physics, 122(10), 10-436. https://doi.org/10.1002/2017JA024482

Wang, R., Nakamura, R., Lu, Q., Baumjohann, W., Ergun, R. E., Burch, J. L., ... & Wang, S. (2017). Electron-scale quadrants of the hall magnetic field observed by the magnetospheric multiscale spacecraft during asymmetric reconnection. Physical Review Letters, 118(17), 175101.

https://doi.org/10.1103/PhysRevLett.118.175101

Wang, X. Y., Lin, Y., & Chang, S. W. (2009). Hybrid simulation of foreshock waves and ion spectra and their linkage to cusp energetic ions. Journal of Geophysical Research: Space Physics, 114(A6). https://doi.org/10.1029/2008JA013745

Wang, Y. L., Elphic, R. C., Lavraud, B., Taylor, M. G. G. T., Birn, J., Russell, C. T., ... & Zhang, X. X. (2006). Dependence of flux transfer events on solar wind conditions from 3 years of Cluster observations. Journal of Geophysical Research: Space Physics, 111(A4). https://doi.org/10.1029/2005JA011342

Yan, G. Q., Mozer, F. S., Phan, T., Shen, C., Chen, T., Bogdanova, Y. V., ... & Liu, Z. X. (2016). Quasi-continuous reconnection accompanied by FTEs during IMF Bz≈ 0 nT observed by Double Star TC-1 at the dawnside magnetopause. Advances in Space Research, 58(2), 208-217. https://doi.org/10.1016/j.asr.2015.08.014

Yao, S. T., Shi, Q. Q., Liu, J., Yao, Z. H., Guo, R. L., Ahmadi, N., ... & Giles, B. L. (2018). Electron dynamics in magnetosheath mirror-mode structures. Journal of Geophysical Research: Space Physics, 123(7), 5561-5570. https://doi.org/10.1029/2018JA025607

Zenitani, S., Hesse, M., Klimas, A., & Kuznetsova, M. (2011). New measure of the dissipation region in collisionless magnetic reconnection. Physical review letters, 106(19), 195003.

https://doi.org/10.1103/PhysRevLett.106.195003

Zhang, Y. C., Lavraud, B., Dai, L., Wang, C., Marchaudon, A., Avanov, L., ... & Torbert, R. (2017). Quantitative analysis of a Hall system in the exhaust of asymmetric magnetic reconnection. Journal of geophysical research: Space physics, 122(5), 5277-5289. https://doi.org/10.1002/2016JA023620

Zhong, Z. H., Zhou, M., Deng, X. H., Song, L. J., Graham, D. B., Tang, R. X., ... & Giles, B. L. (2021). Three-dimensional electron-scale magnetic reconnection in Earth's magnetosphere. Geophysical Research Letters, 48(1), 2020GL090946. https://doi.org/10.1029/2020GL090946

Zhong, Z. H., Lei, G. Y., Zhou, M., Zhang, M., Tang, R. X., Graham, D. B., ... & Khotyaintsev, Y. V. (2023). Observations of Dynamical Flux Ropes and Active Multiple X-Line Reconnection at Earth's Magnetopause. Journal of Geophysical Research: Space Physics, 128(3), e2022JA031091. https://doi.org/10.1029/2022JA031091

Zhou, M., Berchem, J., Walker, R. J., El-Alaoui, M., Deng, X., Cazzola, E., ... & Burch, J. L. (2017). Coalescence of macroscopic flux ropes at the subsolar magnetopause: Magnetospheric Multiscale observations. Physical Review Letters, 119(5), 055101. https://doi.org/10.1103/PhysRevLett.119.055101

Zhou, M., Deng, X. H., Zhong, Z. H., Pang, Y., Tang, R. X., El-Alaoui,

M., ... & Lindqvist, P. A. (2019). Observations of an electron diffusion region in symmetric reconnection with weak guide field. The Astrophysical Journal, 870(1), 34. https://doi.org/10.3847/1538-4357/aaf16f

Zhou, M., Man, H., Yang, Y., Zhong, Z., & Deng, X. (2021). Measurements of energy dissipation in the electron diffusion region. Geophysical Research Letters, 48(24), e2021GL096372. https://doi.org/10.1029/2021GL096372

Zou, Y., Walsh, B. M., Chen, L. J., Ng, J., Shi, X., Wang, C. P., ... & Michael Ruohoniemi, J. (2022). Unsteady Magnetopause Reconnection Under Quasi-Steady Solar Wind Driving. Geophysical research letters, 49(1), e2021GL096583. https://doi.org/10.1029/2021GL096583

Figure 1.

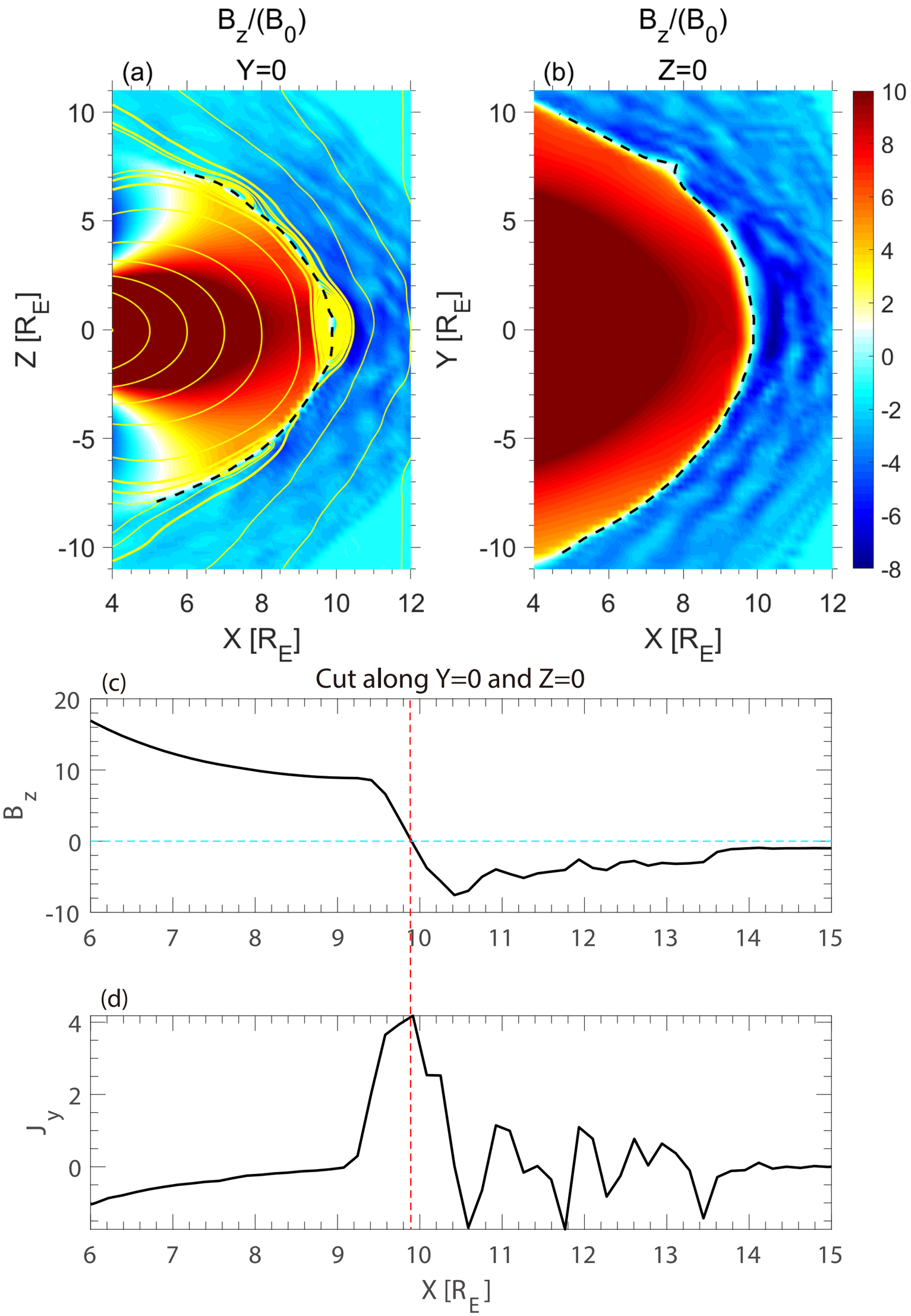
$B_z/(B_0)$
(a)
Y=0
Z [R_E]
X [R_E]
$B_z/(B_0)$
(b)
Z=0
Y [R_E]
X [R_E]
10
8
6
4
2
0
-2
-4
-6
-8
Cut along Y=0 and Z=0
(c)
B_z
(d)
J_y
X [R_E]

Figure 2.

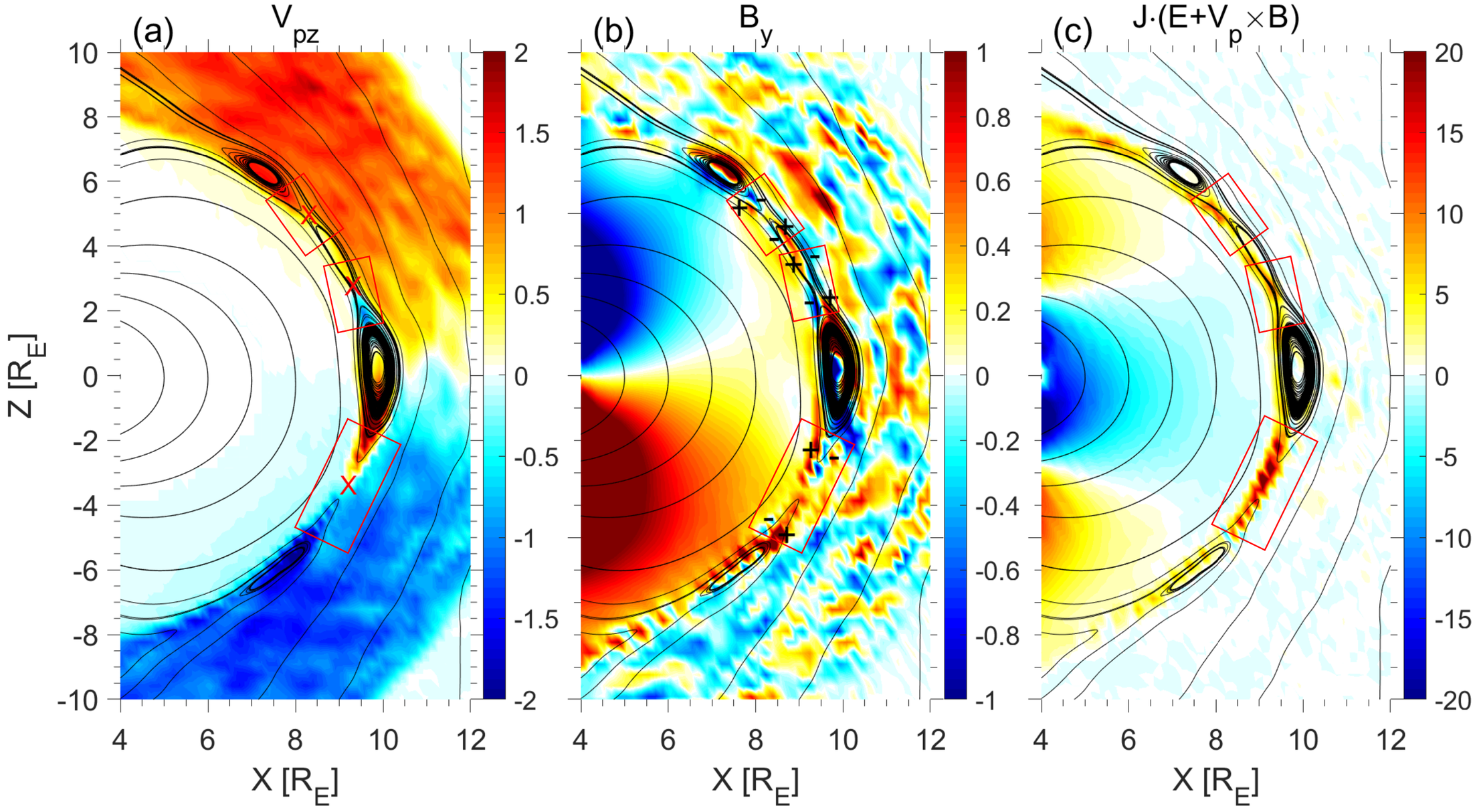
(a)
V_{pz}
(b)
B_y
(c)
$J\cdot(E+V_p\times B)$
Z [R_E]
X [R_E]
X [R_E]
X [R_E]
10
8
6
4
2
0
-2
-4
-6
-8
-10
4
6
8
10
12
2
1.5
1
0.5
0
-0.5
-1
-1.5
-2
1
0.8
0.6
0.4
0.2
0
-0.2
-0.4
-0.6
-0.8
-1
20
15
10
5
0
-5
-10
-15
-20

Figure 3.

B_x=0, B_z=-1

(a) t=005.00

(b) t=020.00

(c) t=060.00

(d) t=100.00

(e) t=145.00

$Z/(R_E)$

$Y/(R_E)$

15 10 5 0 -5 -10 -15

Figure 4.

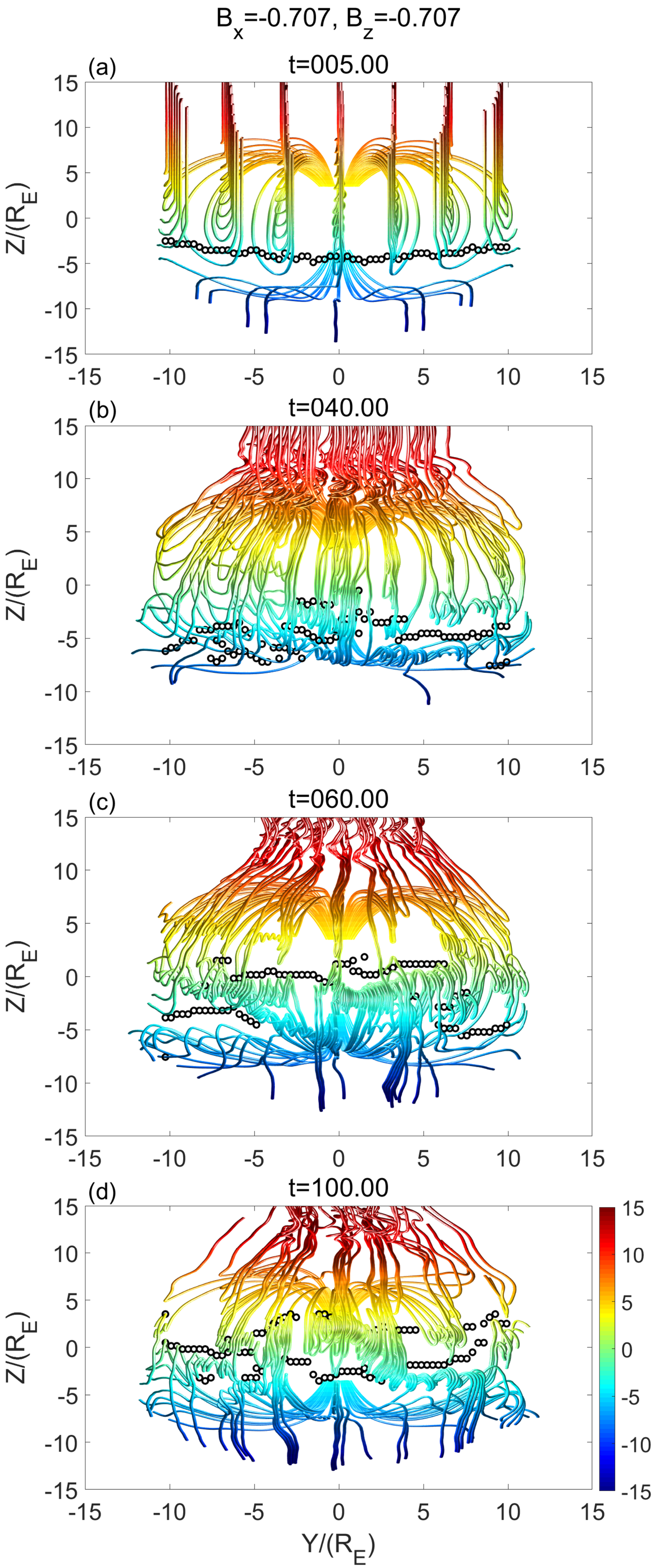
B_x=-0.707, B_z=-0.707
(a)
t=005.00
(b)
t=040.00
(c)
t=060.00
(d)
t=100.00
Z/(R_E)
Y/(R_E)
15
10
5
0
-5
-10
-15

Figure 5.

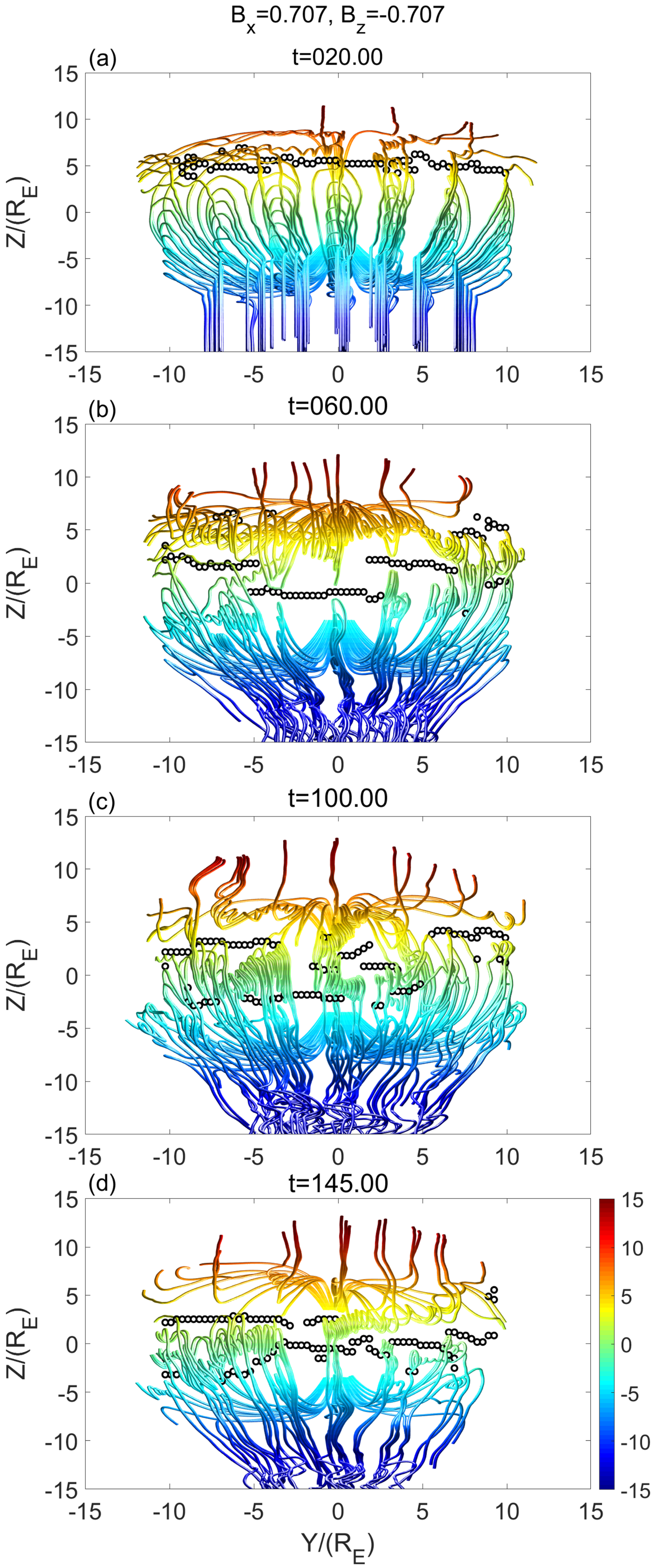
B_x=0.707, B_z=-0.707
(a)
t=020.00
(b)
t=060.00
(c)
t=100.00
(d)
t=145.00
Z/(R_E)
Y/(R_E)
15
10
5
0
-5
-10
-15

Figure 6.

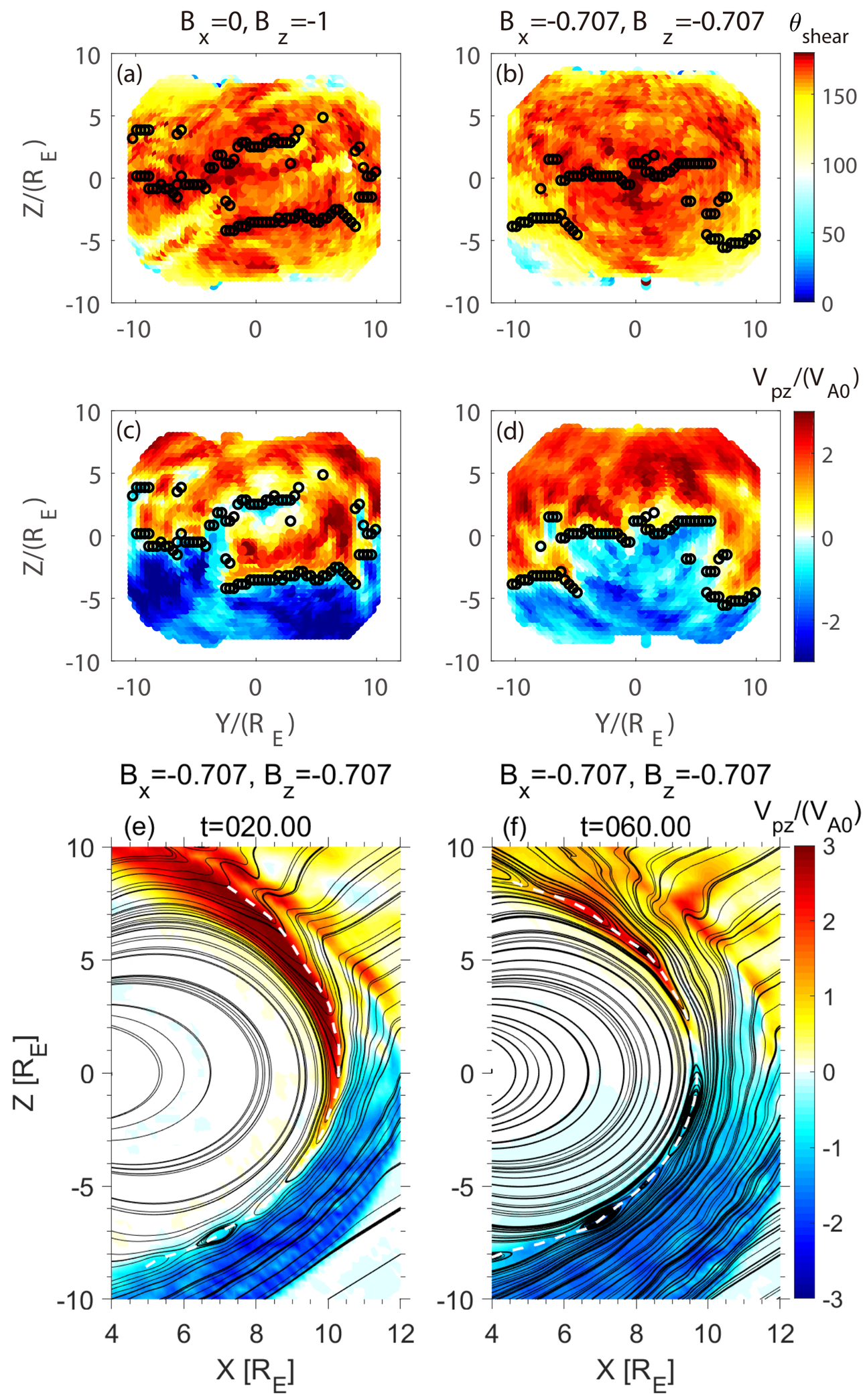
B x =0, B z =-1
B x =-0.707, B z =-0.707
θ shear
(a)
(b)
(c)
(d)
Z/(R E)
Y/(R E)
V pz /(V A0)
B x =-0.707, B z =-0.707
(e) t=020.00
(f) t=060.00
Z [R E]
X [R E]

Figure 7.

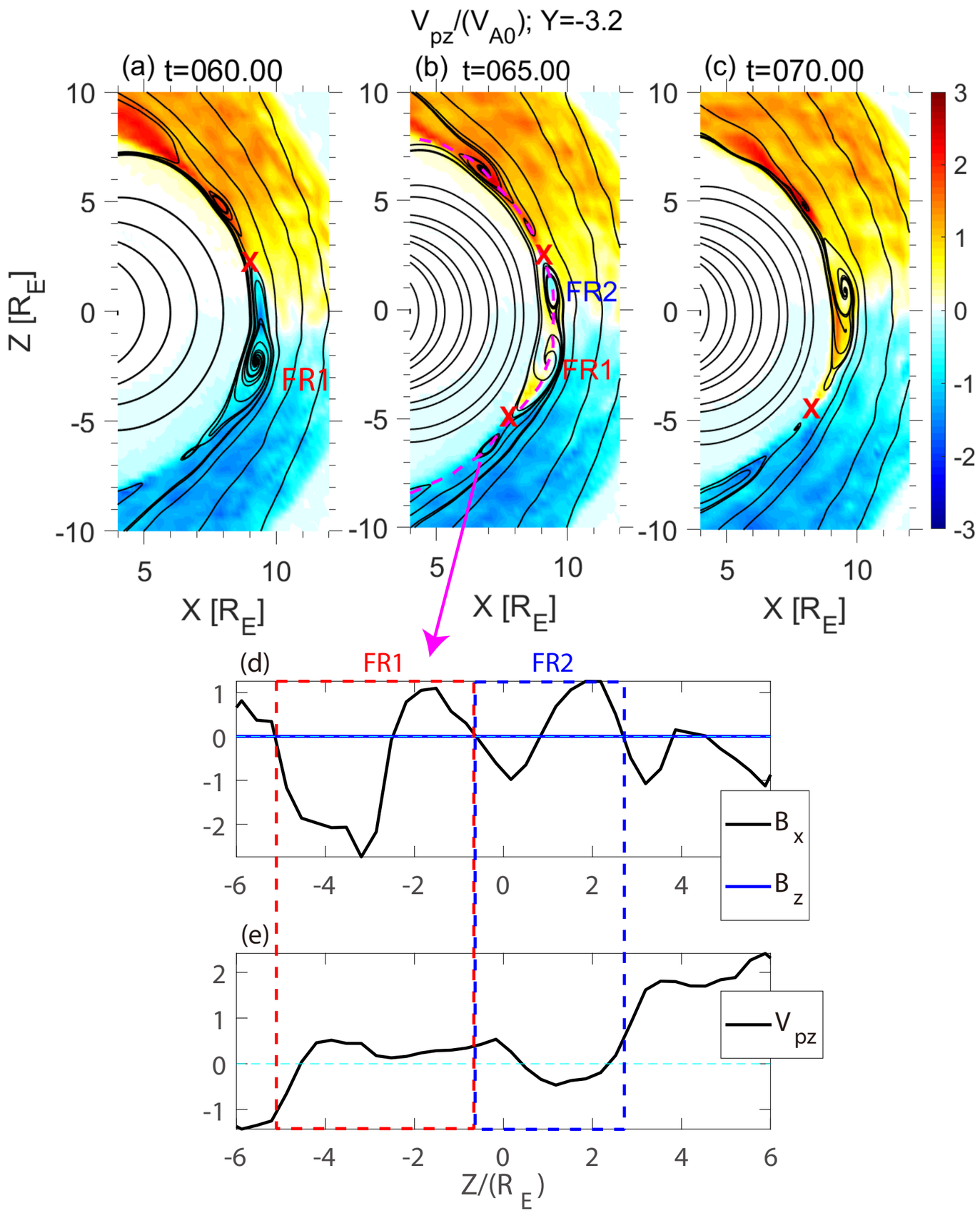
$V_{pz}/(V_{A0})$; Y=-3.2
(a) t=060.00
(b) t=065.00
(c) t=070.00
Z [R_E]
X [R_E]
FR1
FR2
X
(d)
(e)
B_x
B_z
V_{pz}
Z/(R_E)

Figure 8.

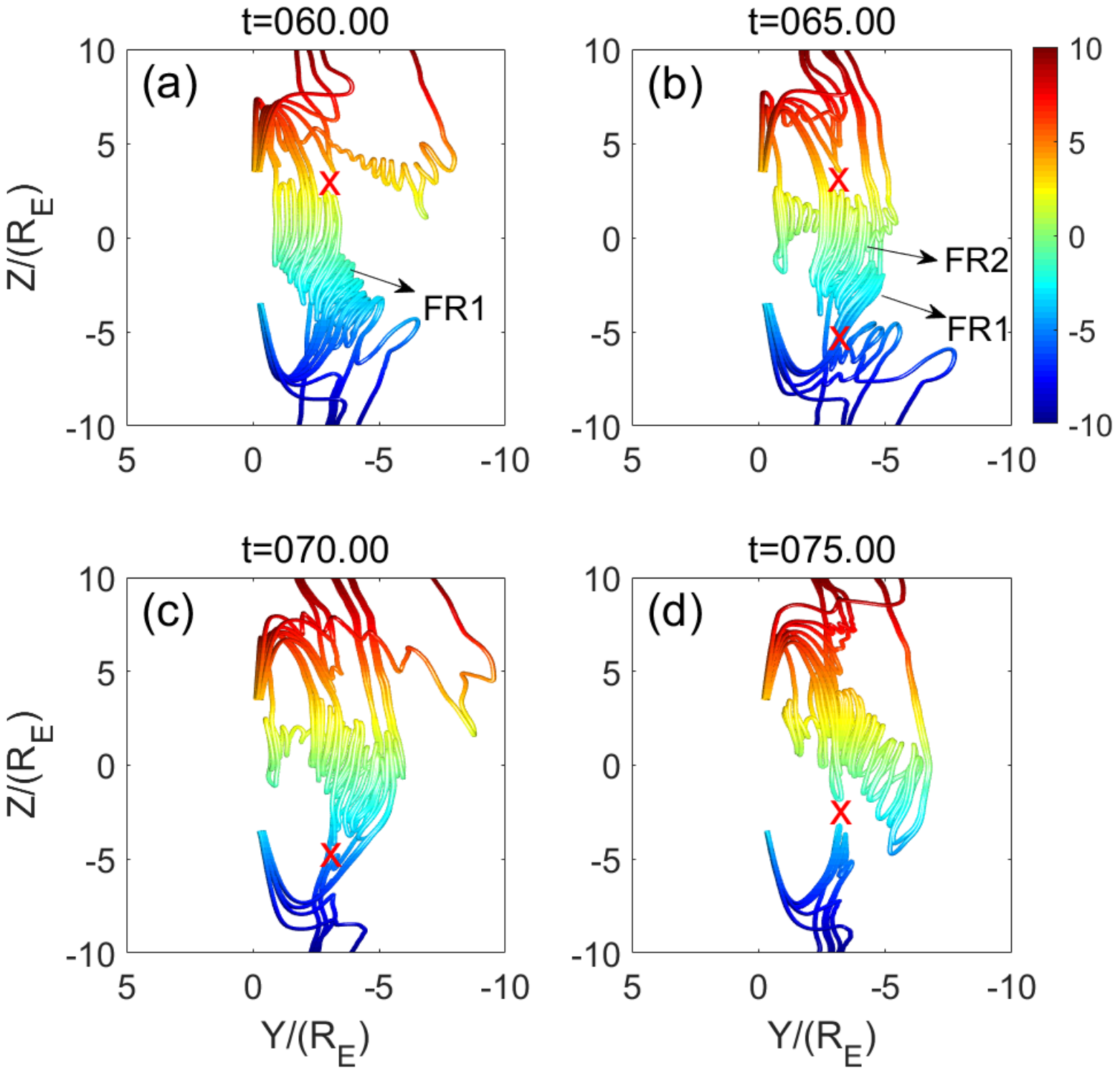
t=060.00
t=065.00
t=070.00
t=075.00
(a)
(b)
(c)
(d)
FR1
FR2
X
10
5
0
-5
-10
Z/(R_E)
Y/(R_E)

Figure 9.

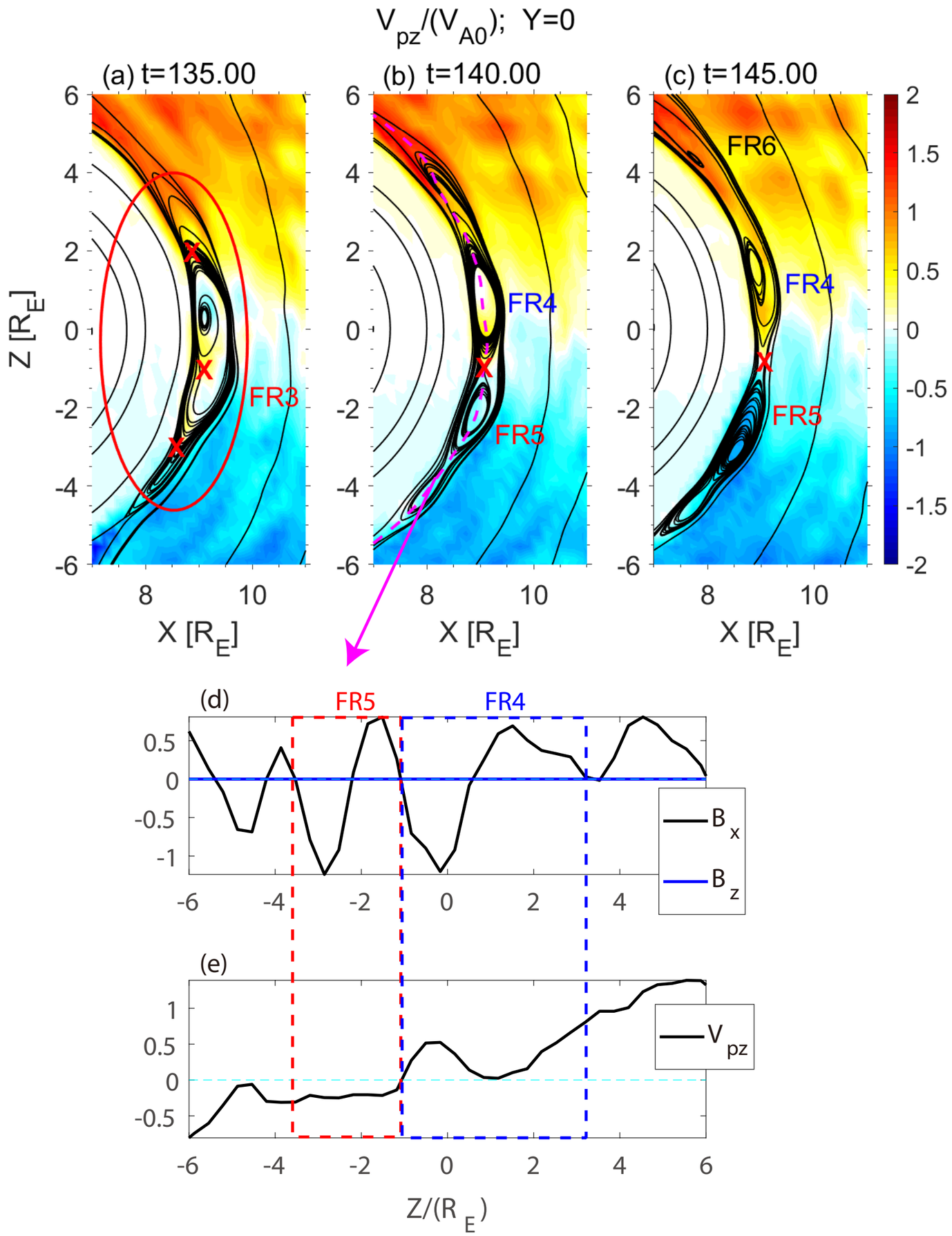
$V_{pz}/(V_{A0})$; Y=0
(a) t=135.00
(b) t=140.00
(c) t=145.00
FR3
FR4
FR5
FR6
Z [R_E]
X [R_E]
(d)
B_x
B_z
(e)
V_{pz}
Z/(R_E)

Figure 10.

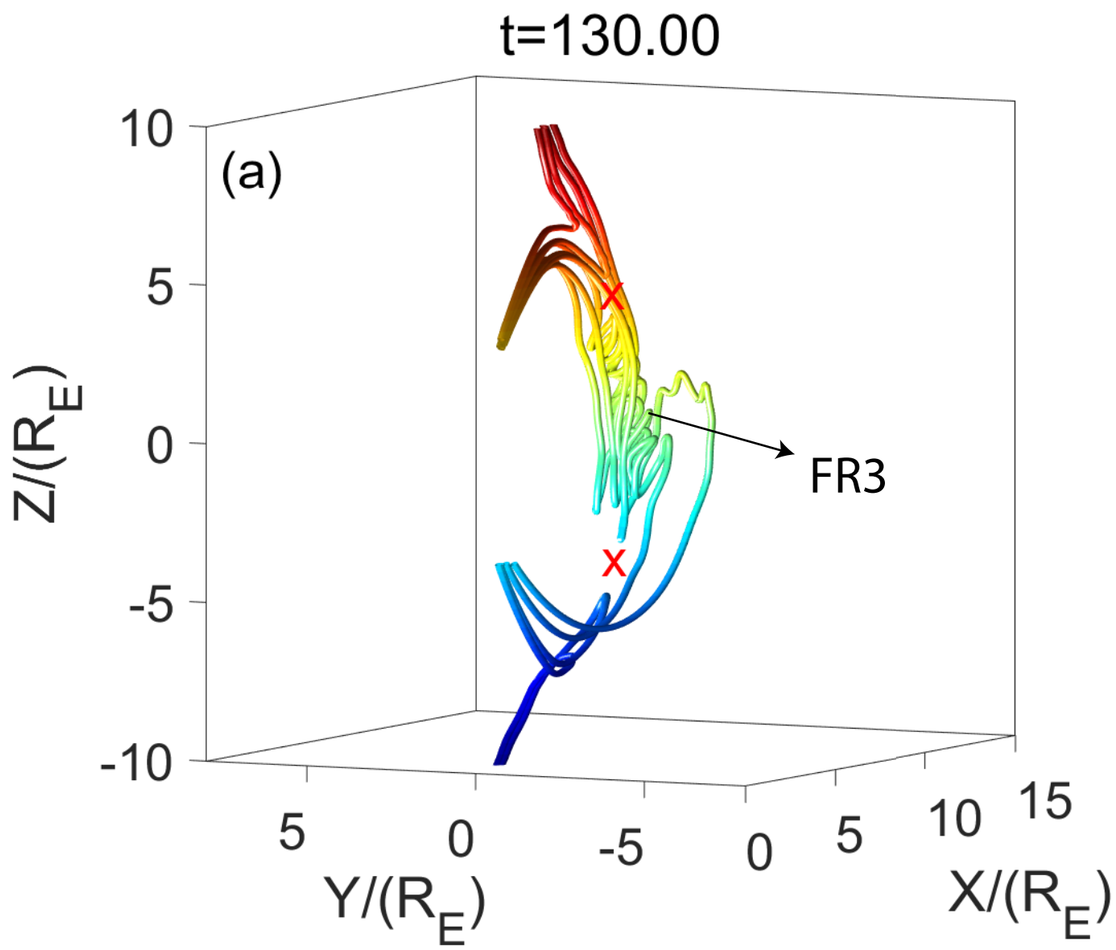
t=130.00
(a)
FR3
X
Z/(R_E)
Y/(R_E)
X/(R_E)

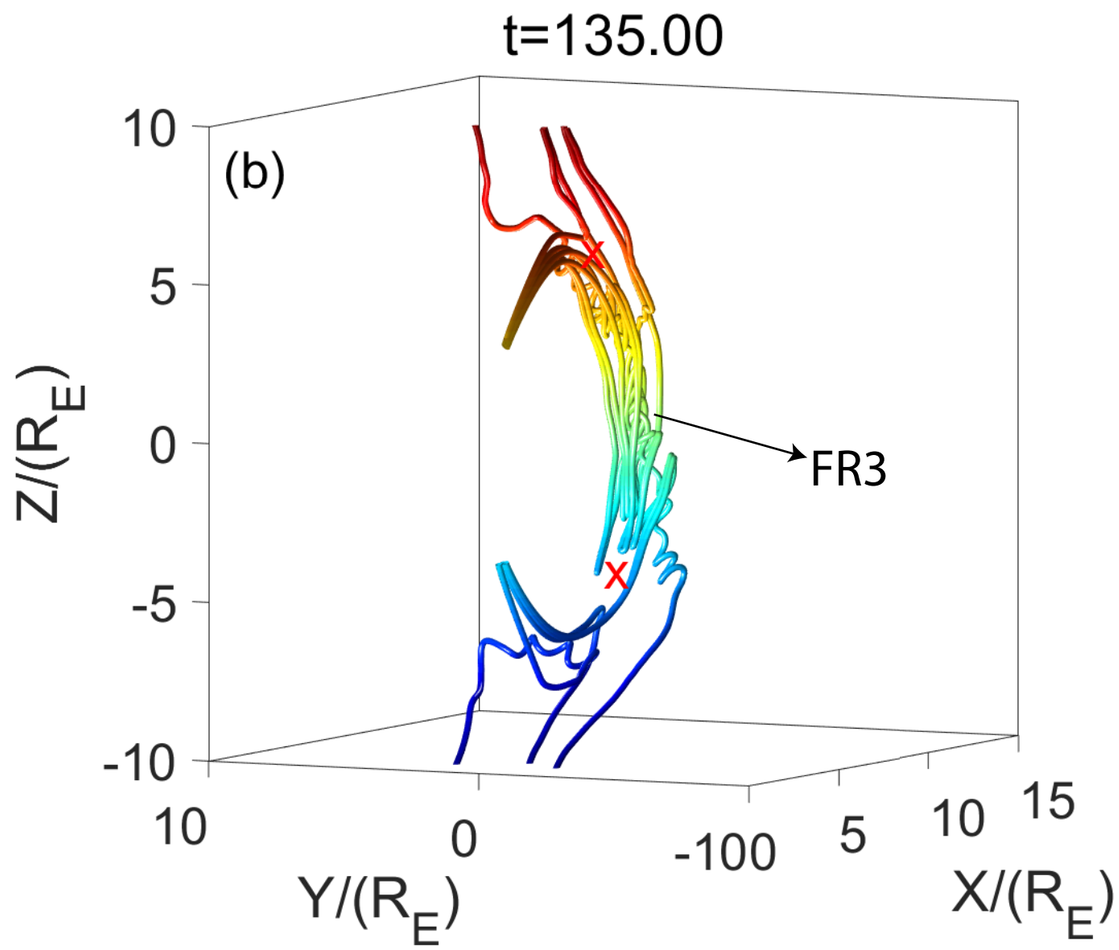
t=135.00
(b)
FR3
X
Z/(R_E)
Y/(R_E)
X/(R_E)

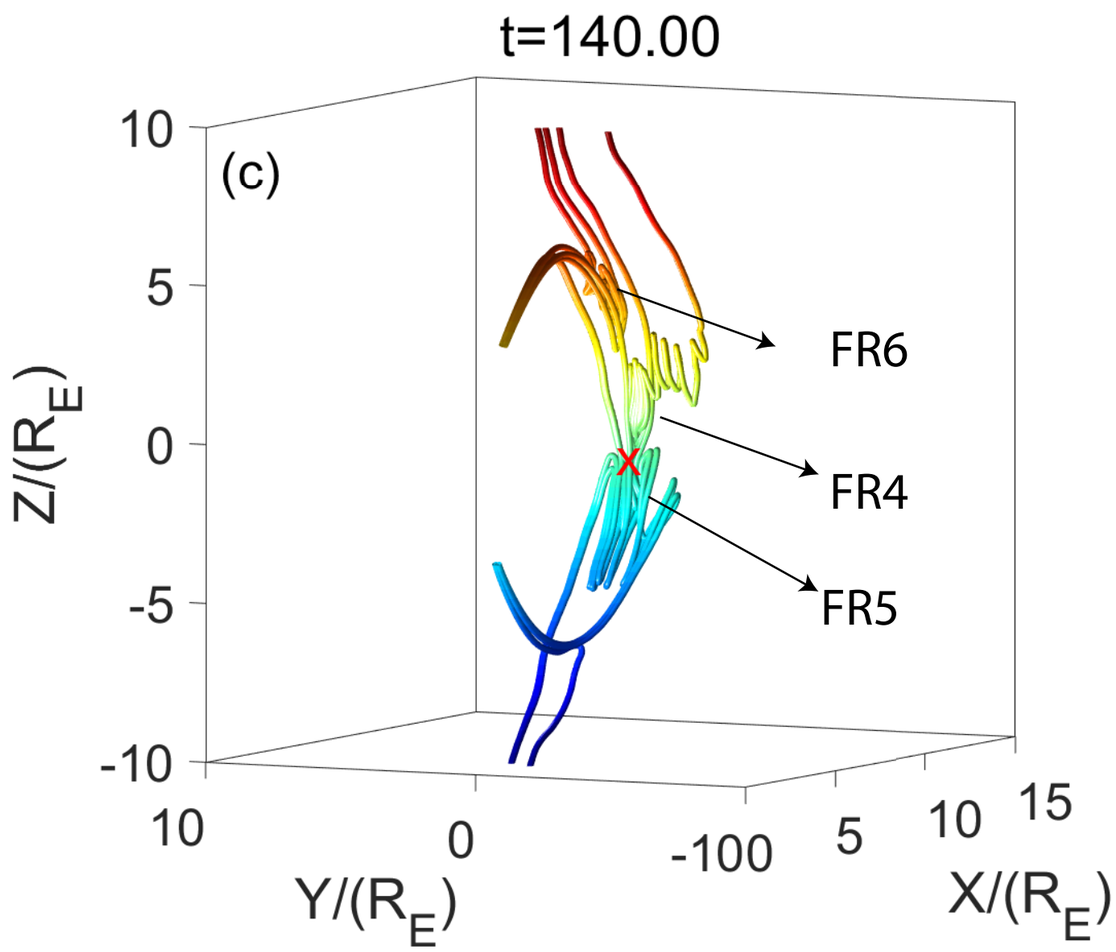
t=140.00
(c)
FR6
FR4
FR5
X
Z/(R_E)
Y/(R_E)
X/(R_E)

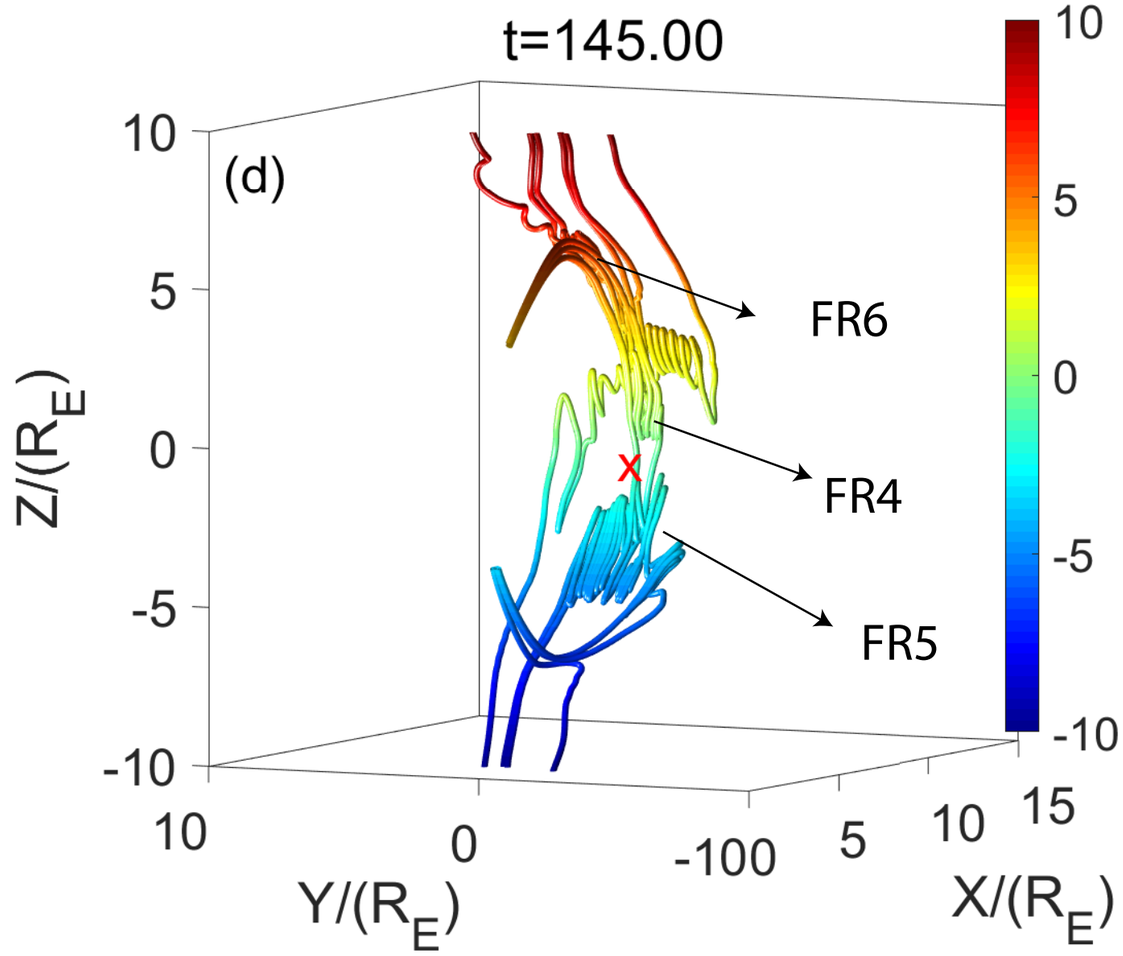
t=145.00
(d)
FR6
FR4
FR5
X
Z/(R_E)
Y/(R_E)
X/(R_E)

Figure 11.

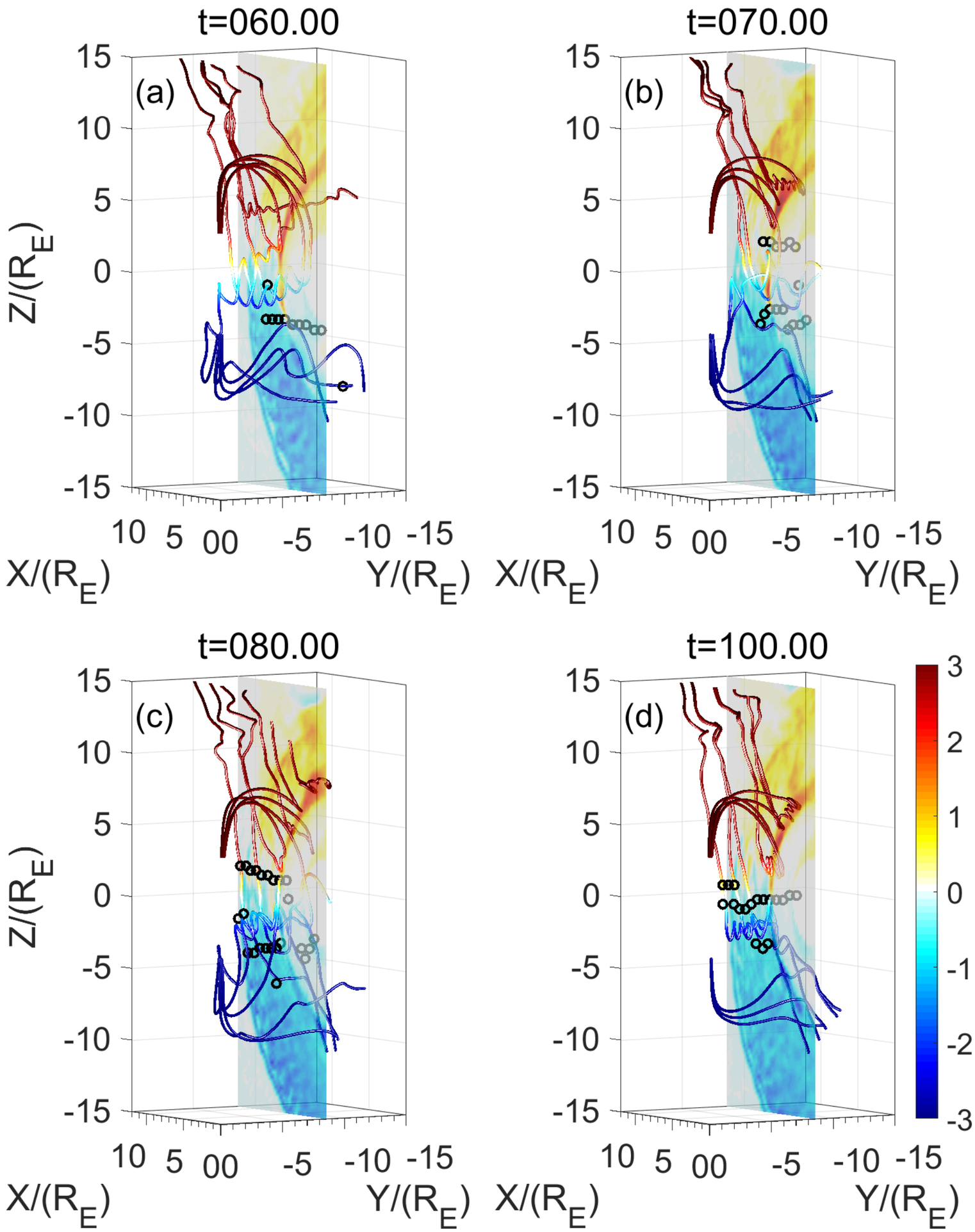
t=060.00
t=070.00
t=080.00
t=100.00
(a)
(b)
(c)
(d)
15
10
5
0
-5
-10
-15
Z/(R_E)
10 5 00 -5 -10 -15
X/(R_E)
Y/(R_E)
3
2
1
0
-1
-2
-3